

WHAT CAUSES SCATTER-FREE TRANSPORT OF NON-RELATIVISTIC SOLAR ELECTRONS?

LUN C. TAN^{1,6}, DONALD V. REAMES², CHEE K. NG^{3,7}, XI SHAO⁴, AND LINGHUA WANG⁵

¹ Heliospheric Physics Laboratory, Code 672, NASA Goddard Space Flight Center, Greenbelt, MD 20771, USA; ltan@mail.umd.edu

² Institute for Physical Science and Technology, University of Maryland, College Park, MD 20742, USA

³ College of Science, George Mason University, Fairfax, VA 22030, USA

⁴ Department of Astronomy, University of Maryland, College Park, MD 20742, USA

⁵ Space Science Laboratory, University of California, Berkeley, CA 94720, USA

Received 2010 June 23; accepted 2010 December 16; published 2011 January 31

ABSTRACT

We have examined the cause of the scatter-free transport of non-relativistic solar electrons. Electron scatter-free transport events are compared with the diffusive transport event. The emphasis of our examination is on the energy dependence of electron angular distributions and the steepening of interplanetary magnetic field (IMF) power spectral densities (PSDs). Near and above the proton gyrofrequency, the effects of both *R*-mode (whistler) and *L*-mode (electromagnetic ion cyclotron, EMIC) waves need to be taken into account separately. The PSD spectral steepening due to the EMIC wave damping by solar-wind thermal ions becomes essential. In a fast-rise–fast-decay impulsive electron event we have observed such steepening, which significantly reduces PSD levels at frequencies above the proton gyrofrequency. The spectral steepening thus produced favors the occurrence of scatter-free transport of low-energy electrons. Consequently, within the *Wind*/3D Plasma and Energetic Particle Instrument/Silicon Semiconductor Telescope measured energy range (~ 25 –500 keV), there appears to be an electron energy window, across which the scatter-free transport of lower energy electrons would change to the diffusive transport of higher energy electrons. We have observed such a change and found it is correlated with the occurrence of broken power-law spectra of electrons. Thus the connection between the transition from diffusive to scatter-free electron transport and the concurrent transition from high to low IMF PSD levels with corresponding breaks in the electron power-law energy spectrum and PSD spectrum has been recognized.

Key words: acceleration of particles – magnetohydrodynamics (MHD) – Sun: coronal mass ejections (CMEs) – Sun: heliosphere – Sun: particle emission

1. INTRODUCTION

1.1. Identification of Scatter-free Transport Periods of Non-relativistic Solar Electrons

The “scatter-free” propagation of solar energetic particles (SEPs) is an important particle transport phenomenon in the interplanetary magnetic field (IMF). In this work, we focus on the scatter-free transport of non-relativistic solar electrons, because we plan to employ them as a probe to detect the topology of magnetic clouds (MCs; Tan et al. 2009). We will keep the sense of scatter-free transport of electrons as in the original paper of Lin (1974), indicating that non-relativistic solar electrons appear to have the scattering mean free path $\lambda \geq 1$ AU in the interplanetary medium (IPM).

During the scatter-free transport periods one may carry out the “flight-time” examination of SEPs. For example, the onset time analysis (e.g., Reames 2009) that is based on the flight-time examination can be used to estimate the solar release time of SEPs and the path length traveled by first arriving particles from the Sun to 1 AU. Since in the pitch-angle distribution (PAD) of solar particles the first arriving particles populate in the $|\mu| \sim 1$ region, where $\mu = \cos(\alpha)$ is the cosine of the particle pitch angle (α), they are suitable for flight-time measurement. In sufficiently intense events only a tiny fraction of the accelerated particles need propagate with $|\mu| \sim 1$ for accurate onset timing.

It is not difficult to identify an electron scatter-free transport period based on the observation of fast-rising–fast-decay impul-

sive electron events, whose intensity–time profile shows a sharp rise and rapid initial decay followed by a long decay. Such a profile implies that electron injection at the Sun is impulsive and nearly symmetric in time, and most of the electrons (those in the peak) propagate through the IMF essentially scatter free (Lin 1974).

On the other hand, without the presence of fast-rising–fast-decay impulsive electron events it is very difficult to decide on an electron scatter-free transport period. For example, it is expected that SEPs could undergo scatter-free propagation inside an MC because of the reduced IMF turbulence level there. However, during the 1998 May 2 MC passage the measured mean free path of SEPs is time dependent within a large variation range (Torsti et al. 2004). Recent observations of anomalous cosmic rays in MCs by Reames et al. (2009) further cast doubt on conventional ideas about the closed field topologies of MCs. We hence need to develop a technique to relate observations of scatter-free and diffusive electron transport to relevant observations of IMF fluctuations.

1.2. Current Understanding on Particle Scattering by IMF Fluctuations

In the standard quasi-linear theory (QLT) of Jokipii (1966) and Hasselmann & Wibberenz (1968), λ is related to the frequency spectral index q of power spectral density (PSD) of IMF fluctuations. Schlickeiser (1988, 1989) deduced an improved expression of λ in QLT:

$$\lambda = \frac{1}{\pi} \frac{3v}{2A} \left[\frac{2}{(2-q)(4-q)} - \frac{(q-1)}{(q-2)} \left(\frac{v}{V_{sw}} \right)^{q-2} \right], \quad (1)$$

⁶ Also at Department of Astronomy, University of Maryland, College Park, MD 20742, USA.

⁷ Also at Space Science Division, Naval Research Laboratory, Washington, DC 20375, USA.

for the $q \neq 2$ case (after the modification made by Tan & Mason 1993), where v is the particle speed, V_{sw} is the solar-wind speed, and

$$A = \frac{\Omega_g^2}{2\pi} \frac{V_{sw}}{v} \frac{p_r}{B^2} \left(\frac{2\pi v_r v}{V_{sw} \Omega_g} \right)^q$$

is the strength of particle scattering, in which B is the mean magnetic field, Ω_g is the particle gyrofrequency, and p_r is the magnetic field PSD given at the reference frequency ν_r (also, see the λ expression for $q = 2$ in Equation (8) of Schlickeiser 1988). Therefore, according to QLT, the scatter-free ($\lambda > 1$ AU) transport could occur when $A \rightarrow 0$ or $q \rightarrow 2$ (e.g., Lin 1974). For *ions*, Tan & Mason (1993) found that nearly scatter-free transport indeed occurs when either the IMF fluctuation level is low or q is near 2.0, although the theoretically predicted λ value is less than the observed one by ~ 1 order of magnitude. For *electrons*, however, to our knowledge there has been no report of the examination of IMF PSD spectra during electron scatter-free transport periods. The 0.1–40 mHz IMF fluctuation spectra measured by Buttigieg et al. (1999) are resonant with relativistic electrons (see later Figure 10 in this paper). Also, there has been no explanation about the common absence of scatter-free transport events of relativistic electrons (Lin 1974).

In recent years, theoretical progress appeared in the investigation of the solar-wind magnetic fluctuations and their interaction with SEPs, including the on-going debates between the “wave” and “turbulence” approaches in the investigation of solar-wind fluctuations and the weight fraction of the “slab” and two-dimensional (2D) components in the three-dimensional (3D) solar-wind turbulence. However, to comment on these issues is beyond the scope of this observational paper. We will only keep a brief introduction of them for interested readers.

In the wave approach (Coleman 1966), IMF fluctuations are thought to consist mostly of waves derivable from magneto-hydrodynamic (MHD) equations. The approach would imply the presence of a deterministic relation between frequency and wave number, i.e., a dispersion relation. In contrast, in the turbulence approach (Coleman 1968; Matthaeus & Goldstein 1982) IMF fluctuations are assumed to be fundamentally nonlinear and interactive, so that the self-organization of fluctuations over a broad range of frequencies is accomplished. Since the fluctuations interact with each other, there is no deterministic correlation existing between frequency and wave number and the only adequate description is a statistical one. It can be seen (e.g., Sahraoui et al. 2009, and references therein) that a scenario of dispersive cascade and dissipation in the solar-wind turbulence appears to be consistent with the kinetic Alfvén wave (KAW) turbulence as predicted by the gyrokinetic (GK) theory. In addition, observations suggest that the energy of the turbulence is only slightly damped at the proton gyroscale and undergoes another dispersive cascade with the electron scaling.

The geometry of solar-wind turbulence in the 3D space is another important issue. The slab model of the turbulence, in which the wave vector is parallel to the IMF, is motivated from the observation of the Alfvén waves propagating along the mean magnetic field. There are suggestions that the solar-wind magnetic turbulence may be a composite of slab and 2D (wave vectors perpendicular to IMF) components (Matthaeus et al. 1990). Evidence (Bieber et al. 1996) indicates that the fractions of the slab and 2D components are $\sim 20\%$ and $\sim 80\%$, respectively. Recently, even more involved models for the turbulence geometry are under discussion (e.g., “critical balance;” see Goldreich & Sridhar 1995; Horbury et al. 2008).

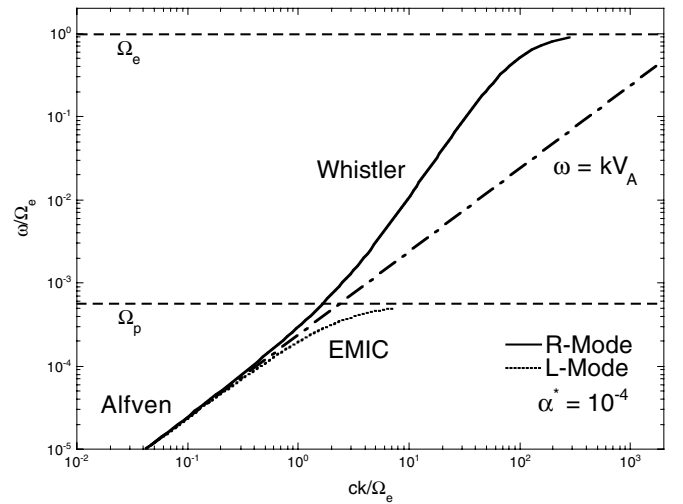


Figure 1. Assuming that in a uniform cold plasma consisting of protons and electrons the electromagnetic waves propagate along the mean magnetic field, their dispersion relations as predicted by classical theory of waves (e.g., Stix 1992) are given in the plasma frame for $\alpha^* = 10^{-4}$ (see the text).

Also, as the magnetic field angle changes from the azimuthal to radial direction, in the magnetometer measurements the relative contribution of the slab component to the 2D component would increase (Bieber et al. 1996). Thus the slab model might provide an approximate solution for the radial field case. In addition, it should be mentioned that the effect of the 2D component on particle scattering has still been unclear. Since the wave vector of the 2D component is perpendicular to the mean field, can it affect the diffusive transport of a particle along the mean field? Also, how representative is the time series of magnetic fluctuations observed on a single spacecraft in characterizing the turbulence field that energetic particles interact with?

For the electrons to experience spatial diffusion, they must be scattered from $\mu > 0$ to $\mu < 0$ and vice versa. In the absence of scattering, the electrons will arrive at 1 AU with $\mu > 0.999$. Although resonance broadening may allow them to cross the region $\mu \sim (-0.3, 0.3)$ (see, e.g., Achatz et al. 1993; Bieber et al. 1994; Ng & Reames 1995; Dröge 2003; Dröge & Kartavykh 2009), there must first be rapid pitch-angle scattering from $\mu \sim 1$ to $\mu \sim 0.3$ against focusing in order for the electrons to access both hemispheres and undergo spatial diffusion. We are hence concerned with the effects in the $\mu > \sim 0.3$ region, in particular, the frequency dependence of electromagnetic wave dispersion relations in the wave approach. Here we still assume that in uniform cold plasma the waves propagate along the mean magnetic field. In the plasma frame the dispersion relation of electromagnetic waves is given by classical theory of waves (e.g., Stix 1992) as shown in Figure 1 for an electron–proton (H) plasma in the typical interplanetary condition observed at 1 AU that $\alpha^* \sim 10^{-4}$, where

$$\alpha^* = \Omega_e^2 / \omega_{pe}^2, \quad (2)$$

where Ω_e and ω_{pe} are the gyrofrequency and plasma frequency of electrons, respectively.

It appears from the figure that only in the very low wave number (k) range the wave mode assumes the dispersion relation of Alfvén waves that

$$\omega = kV_A, \quad (3)$$

where ω is the angular frequency of waves and V_A is the Alfvén speed. As k increases so that ω is close to the proton

gyrofrequency Ω_p , the dispersion relations of both *R*-mode (whistler) and *L*-mode (electromagnetic ion cyclotron, EMIC) waves need to be taken into account separately. Since the interaction of EMIC waves with solar-wind thermal ions would damp the waves, the decrease of wave power densities thus caused would reduce the scattering of electrons.

Therefore, we need to carry out a detailed analysis of IMF fluctuations starting from $\omega \sim \Omega_p$ in the plasma frame, which is equivalent to the wave frequency ν_0 of a few tenths Hz in the spacecraft frame after the Doppler shift of waves (Smith et al. 2006). Hereafter we use the subscript “0” and no subscript to differentiate between the spacecraft frame and the plasma frame. Lin (1974) already mentioned the importance of direct measurement of magnetic field power spectra in the range of $\nu_0 \sim 0.1$ –1 Hz at times of electron events. However, it is surprising that so far no such measurement has been reported. We guess that the reason leading to the lack of such a measurement is probably due to the difficulty in the estimation of global IMF fluctuation distributions, because IMF fluctuation information is mainly provided in the local (~ 1 AU) environment.

However, local IMF fluctuations may play a dominant role in affecting the observed PAD of SEPs, because of the coexistence of the particle adiabatic focusing effect that is due to a significant decrease of IMF magnitude with the increase of the radial distance (r) away from the Sun. The effect essentially always dominates over scattering to give a beam-like PAD implying a nearly scatter-free propagation (Lin 1985). In fact, according to the simulation by Qin et al. (2004) for 1 MeV protons, under the condition of $b/B = 0.1$, where B and b are respectively the mean field strength and turbulence field component, the effect keeps the mean μ value ($\langle \mu \rangle$) of protons at ~ 1 until $r > 0.3$ AU. Also, the analysis of the energy dependence of electron scattering status (see Section 3.3 below) indicates that only IMF fluctuations at $r \geq 0.5$ AU could affect the PAD of solar electrons observed at ~ 1 AU.

Furthermore, since the IMF is frozen into the solar wind, the spatial distribution information on IMF fluctuations can be extracted from their observed temporal variation. It is noticeable that the scatter-free transport of electrons usually occurs during a long period of quiet solar-wind conditions. For example, around the 1999 August 7 impulsive electron event examined by Wang et al. (2006) the IMF PSD spectra measured over a ~ 2 day period were nearly unchanged. Also, during a 30 hr passage of the 1995 October 18–20 MC event (Larson et al. 1997) five solar impulsive electron events were detected, implying a continuous existence of very quiet solar-wind conditions. Under the assumption of the average solar-wind speed from a nearly unchanged IMF fluctuation spectrum lasting for a ~ 1 day period, we can expect that the spectrum is a good representation of IMF fluctuations in a range of $\Delta r \sim 0.3$ AU. Therefore, the locally measured IMF fluctuation spectrum is useful in the examination of scatter-free transport status of non-relativistic solar electrons.

1.3. Working Approach

In view of the initial nature of this research, it is adequate to take the typical event analysis of electron scattering as its first step. We hence compare the fast-rising–fast-decay impulsive electron event with the diffusive electron event. Also, we compare the open field line case with the MC case. In this work, we emphasize the significance of electron anisotropic distributions in understanding the variation of electron scattering status. Also, we pay attention to the analysis of IMF fluctuation

spectra in the dissipation range. Since in both scatter-free and diffusive transport events a time interval of > 5 hr is necessary in order to cover the main portion of intensity–time profiles of electrons with the lowest observed energy (~ 1 keV; see Wang et al. 2006), a minimum sampling period of 5 hr is set for the IMF data with the highest time resolution (96 ms). In the ion case, Ng et al. (2003) predicted the increase of IMF fluctuations after SEP event onset due to the self-generated waves by energetic protons, although the increase is below the typical observed PSD level. In this study, we will investigate whether an enhancement of IMF fluctuation levels can be seen in the electron event. Therefore, we plan to perform a continuous analysis of time development of IMF fluctuation levels during consecutively sampled intervals. The total PSD spectrum of IMF fluctuations is used in our analysis.

Trying to explain the observed result, we note that the wave approach is more manageable than the turbulence approach in mathematical expressions. For example, Dröge (2003, p. 1029) needs to use the argument “electrons simply have less time, because of their higher speed, to ‘feel’ the decaying of the correlations and therefore interact with wave numbers over a smaller range and experience weaker scattering compared to ions of the same rigidity” to qualitatively describe the effect of the dissipation range, while in the wave approach, the dispersion relation of EMIC waves can be used to quantitatively predicate the occurrence of wave damping (see Section 3.2). Therefore, in this work, our attempt to explain new observations is based on a simplified model in the wave approach. Any divergence between the model prediction and the observation would motivate new predictions that are based on an improved wave or turbulence approach.

1.4. Questions to be Addressed in This Work

Through our analysis of electron anisotropic distributions, we will inquire whether observed data show an energy dependence of electron scattering status. If the answer to the question is positive, we will further inquire whether such a dependence is consistent with the frequency dependence of total PSD spectra of IMF fluctuations. Furthermore, we will examine the implication of our observations in understanding the reason of the scatter-free propagation of non-relativistic solar electrons. Also, for the purpose of practical application, we will check to see what the characteristics of the PSD spectra should be during the scatter-free transport period of non-relativistic solar electrons.

Data from the *Wind* and *ACE* spacecraft are used in this work. We first present observed data and event selection. Then we introduce the electron anisotropy analysis and IMF PSD spectral measurement. In addition, we develop model calculations in order to estimate the wave frequency dependence of minimum energies of electrons that are resonantly scattered by the waves. Also, we compare the predicted break frequency of IMF dissipation range with observations. Based on the comparison result, we establish the occurrence condition for scatter-free transport of non-relativistic solar electrons.

2. OBSERVATIONS

2.1. Fast-rise–Fast-decay Impulsive Electron Event

As an example of scatter-free transport periods identified from the fast-rise–fast-decay impulsive electron event we choose the 1999 August 7 event previously examined by Wang et al. (2006). The main feature of the event is that the electron intensity enhancements with a clear velocity dispersion can be seen from

Table 1
IMF and Solar-wind Parameters at 1 AU as Averaged Over Sampled Electron Event Intervals

Parameter	17–22 UT 1999 Aug 7	02–07 UT 2002 Apr 21	15–20 UT 2005 May 31
IMF			
B (nT)	6.3 ± 1.0	6.5 ± 0.5	4.2 ± 1.1
θ_B ($^\circ$)	-14 ± 18	-3 ± 13	11 ± 25
ϕ_B ($^\circ$)	126 ± 7	138 ± 3	87 ± 18
Solar wind			
V_{sw} (km s $^{-1}$)	380 ± 20	460 ± 10	458 ± 3
N_p (cm $^{-3}$)	3.8 ± 1.2	3.3 ± 0.4	7.9 ± 0.9
T (K)	$(6.0 \pm 1.0) \times 10^4$	$(7.3 \pm 2.2) \times 10^3$	$(3.5 \pm 0.9) \times 10^4$
v_{th} (km s $^{-1}$)	31 ± 3	11 ± 2	24 ± 3
Derived			
α^*	$(1.1 \pm 0.1) \times 10^{-4}$	$(1.3 \pm 0.3) \times 10^{-4}$	$(2.5 \pm 1.2) \times 10^{-5}$
β^*	0.73 ± 0.06	0.44 ± 0.10	6.2 ± 7.5
V_A (km s $^{-1}$)	72 ± 4	80 ± 10	33 ± 10
$V_{ph}(\omega_b)$ (km s $^{-1}$)	47 ± 9	38 ± 3	23 ± 5
θ_{Bsw} ($^\circ$)	54 ± 7	42 ± 3	93 ± 18
$\cos\theta_{Bsw}$	0.55 ± 0.09	0.74 ± 0.03	0.38 ± 0.10
PSD of waves			
ν_p (Hz)	$(9.6 \pm 0.2) \times 10^{-2}$	$(9.9 \pm 0.7) \times 10^{-2}$	$(6.3 \pm 1.7) \times 10^{-2}$
ν_e (Hz)	180 ± 30	180 ± 13	120 ± 30
$\nu_{b0, pred}$ (Hz)	0.32 ± 0.06	0.77 ± 0.08	0.27 ± 0.08
$\nu_{b0, obs}$ (Hz)	0.28 ± 0.02	...	0.21 ± 0.05
b_l	-1.66 ± 0.02	-1.53 ± 0.02	-1.71 ± 0.02
b_h	-2.66 ± 0.01	-1.57 ± 0.01	-1.95 ± 0.01
$\log(p_0)_h(=a_h)$	-3.32 ± 0.01	-3.69 ± 0.01	-3.13 ± 0.01

0.4 keV to ~ 300 keV, implying that the scatter-free transport of solar electrons lasted for ~ 5 hr (17:00–22:00 UT). The time profiles of unidirectional intensities ($J_{\mu=0.97}$) of electrons traveling parallel to the mean magnetic field outward from the Sun as observed by the *Wind*/3D Plasma and Energetic Particle Instrument (3DP)/Silicon Semiconductor Telescope (SST; Lin et al. 1995) are shown in the top panel of Figure 2, where the fast-rise–fast-decay feature of $J_{\mu=0.97}$ is clearly seen. In addition, the colored vertical lines denote the 1 AU arrival time (t_p) of peak electron intensities given at different E_e values, from which the electron velocity dispersion indicating that faster electrons arrive at 1 AU earlier than slower electrons is visible. The parent flare of the event is unclear. However, the event onset was associated with a type III radio burst (RB) started at 17:03 UT (the vertical dashed line in the panel). The simultaneous injection of > 25 keV solar electrons occurred later than the burst by ~ 8 minutes. The injection spectra of electrons at different energies as deduced from 1 AU observations are impulsive and nearly symmetric. The path length traveled by particles from the Sun to 1 AU as deduced from the peak times of electrons above 25 keV is $l_0 = 1.19 \pm 0.14$ AU, which is close to the length (1.13 AU) of the Parker spiral line estimated at the observed V_{sw} . The IMF and solar-wind parameters averaged over the sampled 5 hr period are listed in Table 1. During the event period, the *Wind* spacecraft was located at $(X_{gse}, Y_{gse}, Z_{gse}) = 115.0, 30.5, 8.1$ [R_E], in comparison with $(X_{gse}, Y_{gse}, Z_{gse}) = 248.8, 9.1, 22.1$ [R_E] of the *ACE* spacecraft, where R_E is Earth’s radius. The distance between the two spacecraft was $\sim 140 R_E$.

2.2. Magnetic Cloud Event

As an example of MC events we choose the 2002 April 21 event, which is one of the large gradual SEP events observed in the solar cycle 23. The event, which shows high-intensity and long-duration enhancements of both ions and electrons, is examined in Tylka et al. (2005, 2006) and Tan et al. (2008, 2009). The event is related to a coronal mass ejection (CME) that was a

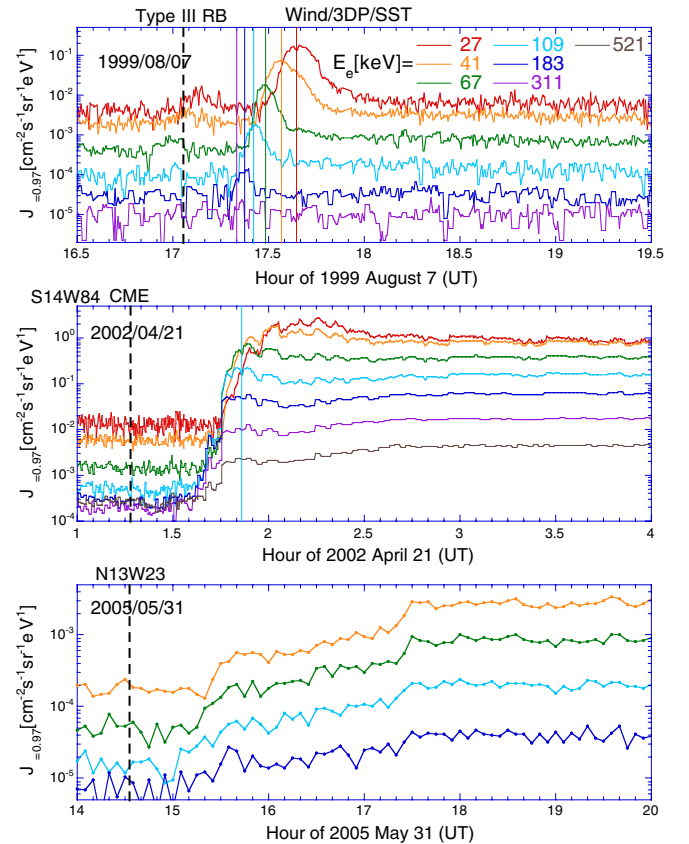


Figure 2. Time profiles of *Wind*/3DP/SST unidirectional intensities ($J_{\mu=0.97}$) of electrons traveling parallel to the mean magnetic field outward from the Sun are shown for the sampled three events, where the vertical dashed line denotes the parent flare, its related RB or CME. The vertical colored lines represent the 1 AU arrival time of $J_{\mu=0.97}$ peak intensities given at different electron energies. The time resolution of the 2005 May 31 event data has been reduced to 5 minutes.

fast (2400 km s⁻¹) halo event associated with an X1.5/1F flare at S14W84. While the flare started at 00:43 UT, the CME had an onset time of 01:16:43 UT (the vertical dashed line on the panel). In addition, the MC passed the *Wind* spacecraft between 2002 April 20 12:00 and 2002 April 21 18:00 UT (Richardson & Cane 2010). During the event period, the bi-directional energetic electron flux lasted for longer than 5 hr. The time profiles of $J_{\mu=0.97}$ for the event are shown in the middle panel of Figure 2, where the electron velocity dispersion is visible. However, the peak of $J_{\mu=0.97}$ can be best identified only at $E_e = 109$ keV. The IMF and solar-wind parameters averaged over the sampled 5 hr period are given in Table 1, from which very low proton temperature (T) and plasma beta (β^*) values inside the MC are seen. The counter-streaming electron beam was also seen through the event, indicating the presence of the outer reflecting boundary of SEPs. Since there may be a very quiet solar-wind environment during the MC period, the event is suitable for the examination of electron scatter-free transport inside an MC. During the event period, the *Wind* spacecraft was located at $(X_{\text{gse}}, Y_{\text{gse}}, Z_{\text{gse}}) = 4.7, 223.0, 10.4$ [R_E], in comparison with $(X_{\text{gse}}, Y_{\text{gse}}, Z_{\text{gse}}) = 223.8, 25.6, -22.8$ [R_E] of the *ACE* spacecraft. The distance between the two spacecraft was $\sim 300 R_E$.

2.3. Diffusive Electron Events

The 2005 May 31 event is used to examine the possible correlation of electron PADs with the locally measured magnetic field PSDs. In addition, during the event period the “size” of magnetic flux tubes can be estimated by comparing the PSD spectra measured by *Wind* and *ACE* when they are well separated. The event is a weak event with limited energy channels having responded. The intensity–time profile of $J_{\mu=0.97}$ in the event is given in the bottom panel of Figure 2, which shows a slower rising (lasting for ~ 3 hr) of $J_{\mu=0.97}$ in contrast to the faster rise of $J_{\mu=0.97}$ in the 1999 August 7 event. The parent N13W23 flare started at 14:33 UT. The *Wind* spacecraft was located at $(X_{\text{gse}}, Y_{\text{gse}}, Z_{\text{gse}}) = 227.1, 99.6, 8.8$ [R_E], while the *ACE* spacecraft was at $(X_{\text{gse}}, Y_{\text{gse}}, Z_{\text{gse}}) = 248.3, -18.7, 0.7$ [R_E]. The distance between the two spacecraft was $\sim 120 R_E$.

2.4. Use of Anisotropy Data to Examine Electron Scattering Status

2.4.1. Energy Dependence of Pitch Angle Distributions of Incident Electrons in the Fast-rise–Fast-decay Impulsive Event and Magnetic Cloud Event

For the 1999 August 7 fast-rise–fast-decay impulsive electron event Wang et al. (2006) observed that at $E_e > 25$ keV the short-duration (8–12 minutes) injection of electrons at different energies is simultaneous. Thus the peak electron intensity (J_{ep}) spectrum could be representative of the injection electron spectrum provided that the scattering in the IPM has the same spatial dependence for all electron energies (Lin 1974; Krucker et al. 2009). Because of velocity dispersion, the 1 AU arrival time (t_p) of peak electron intensities is a function of E_e . Therefore, in order to deduce the peak electron intensity spectrum we first need to determine t_p as a function of E_e from the time profile of the unidirectional intensities ($J_{\mu=0.97}$) of electrons traveling parallel to the mean magnetic field outward from the Sun as measured by *Wind*/3DP/SST (see Figure 2). For the August event, the plot of t_p against $1/v$ over the $E_e = \sim 25$ –250 keV range gives $l_0 = 1.24 \pm 0.06$ AU, which is consistent with $l_0 = 1.19 \pm 0.14$ AU deduced by Wang et al. (2006) in similar

conditions. Since this derived path length is consistent with the length of the Parker spiral line during the event period, most electrons (those in the peak) in this event propagated scatter free in the IPM over a time interval of several hours. Further, the electron velocity dispersion is used to estimate the t_p value at $E_e = 311$ keV, where the intensity peak of electrons is unclear (see below). At a given E_e value we then pick up the $J_{\mu=0.97}$ data measured within a time interval of $t_p(E_e) \pm 4\tau$ to construct the PAD of J_{ep} . With $\tau \sim 25$ s in most cases, the width of the sampling interval is ~ 2.5 minutes.

Here we explain how PADs (i.e., J_{ep} as a function of μ) are generated from *Wind*/3DP/SST data. As described in Tan et al. (2009), the electron intensity J_e recorded in 48 2D angular bins is sorted to the 1D pitch-angle sector having an angular width of 22.5° . Thus the final PAD consists of eight sectors, whose central value is $\alpha_0(j) = 11.25 + 22.5 \times (j-1)^\circ$, where $j = 1, 8$. Since 8 out of 48 angular bins have much small geometrical factors, they are not considered in data reduction. As a result, there are $40/8 = 5$ angular bins entering into one sector in average. We hence need to calculate the electron intensity (J_{em}) and pitch-angle (α_m) values averaged over a sector. Because of the time variation of the magnetic field direction, the angular bins entering into a given pitch-angle sector (j) are time dependent, leading to the time variation of $\alpha_m(j)$ value. The $\alpha_m(j)$ value is different from the nominal value $\alpha_0(j)$, although the difference between them is less than the α_0 difference between two adjacent sectors. Further, over an 8τ sampling interval we have $8+1 = 9$ observed J_{em} versus α_m data points falling into one pitch-angle sector. Since these data points tend to be concentrated near α_0 , there are gaps in the observed PAD. Nevertheless, the gaps do not affect the examination of global characteristics of PADs. Furthermore, when $\alpha_0(j)$ is converted to $\mu_0(j) = \cos(\alpha_0(j))$, the distribution of observed data along the μ -axis is further deformed. For example, because of $\mu_0(1) = 0.98$ and $\mu_0(2) = 0.83$ the data within the pitch-angle sectors of $j = 1$ and 2 would be overlapped. Consequently, the observed number of data clusters could be less than 8. For the 1999 August 7 event, our deduced PAD of J_{ep} is shown in Figure 3, where from top to bottom E_e is counted along an ascending order with the sampling interval denoted at the upper left corner of each panel. We have carried out the background correction by first calculating the PAD of background electrons from pre-event electron data. Each observed J_{ep} value is then subtracted by the corresponding background value given at the same μ value.

In addition, in *Wind*/3DP/SST a fraction of incident electrons would scatter out and deposit only part of their energy at channels lower than the incident energy. In this study, this contamination has been corrected. In order to test the correction effect in Figure 3 the J_{ep} data corrected for the electron deposit energy loss are denoted by solid dots, while the uncorrected data are denoted by open circles. It can be seen that the influence of electron deposit energy loss correction to the PAD at the *peak* of electron intensities is very small, although the correction may be dramatic during the *rise* phase. In order to emphasize the difference, we compare the onset parameter estimated with and without the correction in the 2001 September 24 event as examined in Tan et al. (2009). For incident electrons, the corrected data give $l_0 = 1.6 \pm 0.1$ AU and $t_0 = 10.52 \pm 0.04$ hr, while the uncorrected data give $l_0 = 1.4 \pm 0.2$ AU and $t_0 = 10.60 \pm 0.06$ hr. On the other hand, the *Wind* and *Solar and Heliospheric Observatory (SOHO)* ion data give $l_0 = 1.8 \pm 0.2$ AU and $t_0 = 10.6 \pm 0.1$ hr. Therefore, only the corrected

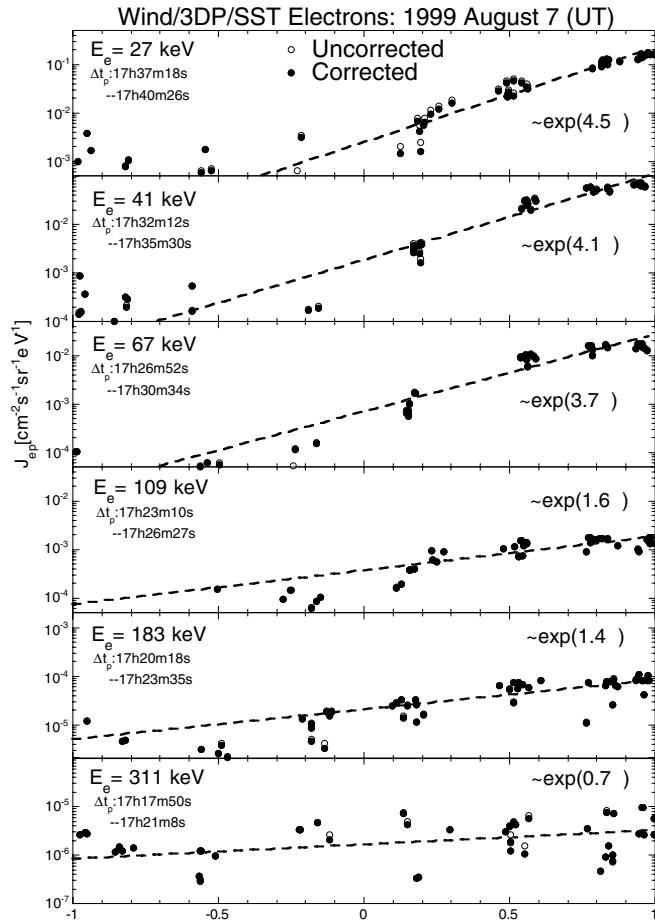


Figure 3. *Wind*/3DP/SST peak electron intensity (J_{ep}) measured at different electron energies (E_e) is plotted against the electron pitch angle cosine (μ) in the 1999 August 7 fast-rise-fast-decay impulsive event, where Δt_p is the sampling time interval of J_{ep} . The dashed line is the exponential ($J_{ep} \propto \exp(\alpha_p \mu)$) fit of J_{ep} data at $\mu > 0$.

electron data provide the l_0 and t_0 values that are consistent with ions within the error range.

In Figure 3, the dashed line is the exponential fit of J_{ep} versus μ for the observed J_{ep} data at $\mu > 0$:

$$J_{ep} = J_{ep0} \exp(\alpha_p \mu), \quad (4)$$

where J_{ep0} is the J_{ep} value given at $\mu = 0$ and α_p is a constant characteristic of the width of PAD of peak incident electrons. While we only used J_{ep} data at $\mu > 0$ in the fitting process, the exponential function (Equation (4)) fits the observed J_{ep} data at $\mu < 0$ reasonably well. From the figure it can be seen that the α_p value decreases from 4.5 at $E_e = 27$ keV to 0.7 at $E_e = 311$ keV.

In the 1999 August 7 impulsive electron event, the electron injection at the Sun is impulsive and nearly symmetric (Wang et al. 2006), so the observed time profiles of electron intensities exhibit prominent peaks at all electron energies. In contrast, in the 2002 April 21 gradual SEP event the continuous electron injection leads to extended time profiles of electron intensities with ambiguous maxima. As a result, in the middle panel of Figure 2 the clearest peak of $J_{m=0.97}$ can be best seen at $E_e = 109$ keV (light blue line), indicating a significant injected electron component from the Sun.

Here we are concerned with the injected electron component that arrived at 1 AU and caused the $E_e = 109$ keV electron peak at the time denoted by the light blue line in the middle

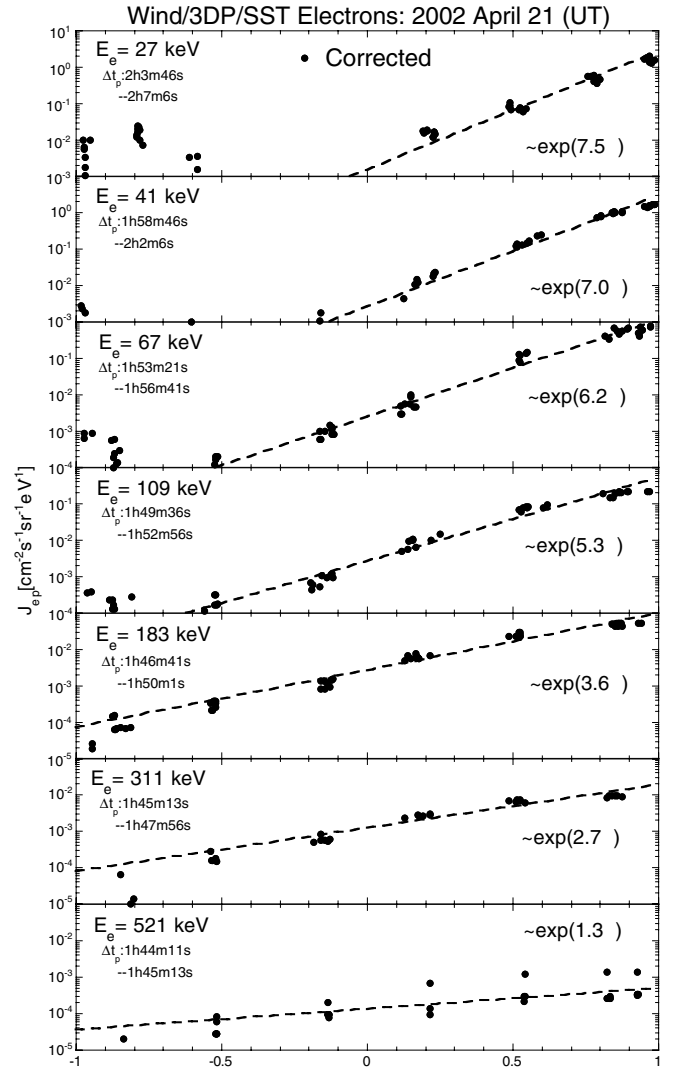


Figure 4. Same as Figure 3, but for the 2002 April 21 MC event. The dashed line is the exponential fit of J_{ep} data at $\mu > -0.5$.

panel. What are the 1 AU arrival times of such injected electron components at other energies? Since, under the scatter-free transport assumption, the arrival time difference between E_e and $E_e = 109$ keV electrons is only dependent upon the path length l_0 , the difference should be same between the 1999 August 7 and 2001 April 21 events if their l_0 values are same.

By using ion data from the *Wind*/Energetic Particles: Acceleration, Composition, and Transport (EPACT) Experiment/Low-Energy Matrix Telescope (LEMT; von Rosenvinge et al. 1995) and electron data from *Wind*/3DP/SST at $E_e > 100$ keV, we deduce $l_0 = 1.27 \pm 0.02$ AU from the onset time analysis of the 2001 April 21 event, which is consistent with $l_0 = 1.24 \pm 0.06$ AU for the 1999 August 7 event (see above). Therefore, we can use the observed time difference between E_e and $E_e = 109$ keV electrons in the 1999 August 7 event (upper panel) to determine the differences in the 2001 April 21 event, and hence the 1 AU arrival time of our electron component of interest is denoted at the upper left corner of each panel in Figure 4.

In Figure 4, the dashed line is the exponential fit of J_{ep} versus μ for the observed J_{ep} data at $\mu > -0.5$. It can be seen from the figure that the exponential approximation is well kept in the April event, although at lower energies some reflected electrons

may appear in the $\mu < 0$ region (Tan et al. 2009). There is a decrease of the α_p value from 7.5 at $E_e = 27$ keV to 1.3 at $E_e = 521$ keV.

2.4.2. Implication of the Change of Electron Pitch Angle Distributions

Here we explore the implication of the change of α_p in understanding the transition of electron scattering status that is usually characterized by λ . The scatter-free transport event has $\lambda > 1$ AU, in comparison with the diffusive transport event with $\lambda < 0.2$ AU. Historically, λ is defined under the quasi-static approximation of the Fokker–Planck equation in the standard QLT (e.g., Jokipii 1971). It is less effective to describe weak scattering events. Bieber et al. (1996) noted that the fitting procedure based on the comparison of intensity–time and anisotropy–time profiles of SEPs with the prediction of the focused transport equation (Roelof 1969) does not yield a meaningful finite value of λ for such events. They hence simply set $\lambda = 1.25$ AU for the nearly scatter-free transport events observed at 1 AU. Similarly, here we will not calculate the λ value of nearly scatter-free transport events by using the focused transport equation. Instead, since we are concerned with the electron energy at which the scatter-free transport status of lower energy electrons changes to the diffusive transport status of higher energy electrons, it is more important to estimate the λ value of higher energy electrons based on the diffusion–convection equation. Because of the higher speed of electrons, however, the solar-wind convection effect is negligible. Consequently, the Parker diffusive model (Parker 1963) is useful in the estimation of the λ value of higher energy electrons based on the peak electron spectral measurements. The Parker model is often applied to understand the physical implication of simulation results (e.g., Ng & Reames 1994; Ng et al. 2003).

Since an observer at 1 AU would see different PADs of particles in different scattering events, it is expected that PAD could be used to characterize the scattering status of particles. However, PAD is time dependent during the developing process of an SEP event. For example, in an impulsive event the particle anisotropy observed at 1 AU decays monotonically from a high initial value. Therefore, even in a diffusive event with $\lambda < 0.2$ AU a sharply anisotropic PAD can be seen during the early stage of its onset phase when the arriving particles have not been scattered or only scattered once.

Nevertheless, it is possible to find a criterion to characterize the whole event as scatter free or diffusive. In fact, the spherically symmetric radial diffusion model with an impulsive electron injection (Parker 1963) predicts that at the peak time t_p the particle anisotropy

$$\xi(t_p) = 3\lambda_r r^{(\beta-1)}, \quad (5)$$

where r is the radial distance and the radial mean free path $\lambda_r = \lambda_{r0} r^\beta$, λ_{r0} and β being constants. We will use this equation to motivate the anisotropy criterion of diffusive transport event at the peak time. For an observer at $r = 1$ AU, it implies that $\lambda_r < 1$ AU for the diffusion picture to apply, because $\xi(t_p)$ must always be less than 3. Furthermore, since for true diffusion the observed particles must perform at least a few random walks, we adopt $\xi(t_p) < 1.5$ (for $\lambda_r < 0.5$ AU) to characterize the diffusive phase of a particle event. For $J_{ep} \propto \exp(\alpha_p \mu)$ (Equation (4)), $\alpha_p = 1.5$ gives $\xi = 3(\mu J_{ep})/(J_{ep}) = 1.31$, the antisunward to sunward particle flux ratio = 7.33, and the antisunward-to-sunward particle number ratio of 4.48. These ratios show that, despite the apparently large anisotropy ξ , there are a significant

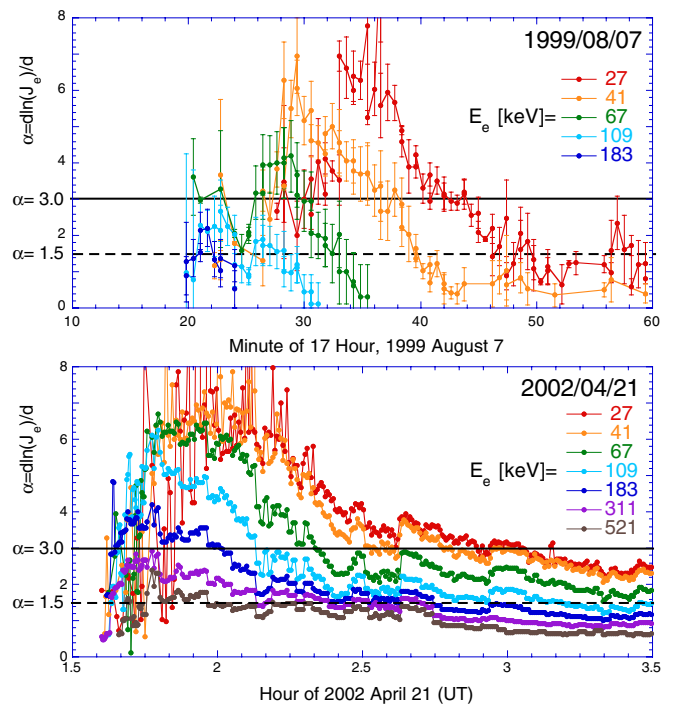


Figure 5. Time profiles of $\alpha = d\ln(J_e)/d\ln(\mu)$ for the 1999 August 7 impulsive electron event (upper panel) and 2002 April 21 MC event (lower panel).

number of particles in the sunward ($\mu < 0$) hemisphere or significant sunward particle flux. Therefore, one way to establish the transition of scattering status is to show the time history of particle anisotropy. Similar to Equation (4) for α_p measured at the peak time t_p , we define α measured at time t from

$$J_e = J_{e0} \exp(\alpha \mu), \quad (6)$$

where J_{e0} is the J_e value given at $\mu = 0$. If $\xi > 2$ or $\alpha > 3$ for a given particle energy channel during the entire period of interest, then we find for scatter-free transport event. On the contrary, if ξ falls to < 1.31 or α falls to < 1.5 during that period, we find for diffusive transport event.

In Figure 5, we show the time profiles of α at different energies of electrons in the 1999 August 7 and 2002 April 21 events on the upper and lower panels, respectively. Here we use the horizontal solid and dashed lines to denote $\alpha = 3$ and $\alpha = 1.5$, respectively. Since the 1999 August 7 event is an impulsive electron event, for the electrons detected by the *Wind*/3DP/SST sensor ($E_e \sim 25$ –500 keV) its fast-rising–fast-decay portion lasted for less than 1 hr (note that the justification of scatter-free status during a ~ 5 hr period in the August event is based on the observation of ~ 1 keV electrons; see Wang et al. 2006). Nevertheless, the decrease of α with time is clearly seen in the upper panel. During the main portion of the event we have $\alpha > 3$ at $E_e < 60$ keV and $\alpha < 1.5$ at $E_e > 120$ keV. Therefore, in the 1999 August 7 event the electron scattering status changes from scatter free to diffusive between $E_e = 60$ and 120 keV.

Since the increase of electron intensities in the 2002 April 21 MC event lasted longer, we show the time profile of α during the first 2 hr of the event in the lower panel of Figure 5. Similar to the 1999 August 7 impulsive electron event, we see the decrease of α with time in this MC event. During the main portion of the event, however, we have $\alpha > 3$ at $E_e < 250$ keV and $\alpha < 1.5$ at $E_e > 500$ keV, indicating that the change of electron scattering status from scatter free to diffusive occurs between $E_e = 250$ and 500 keV. Therefore, in the 2002 April 21 MC event our deduced

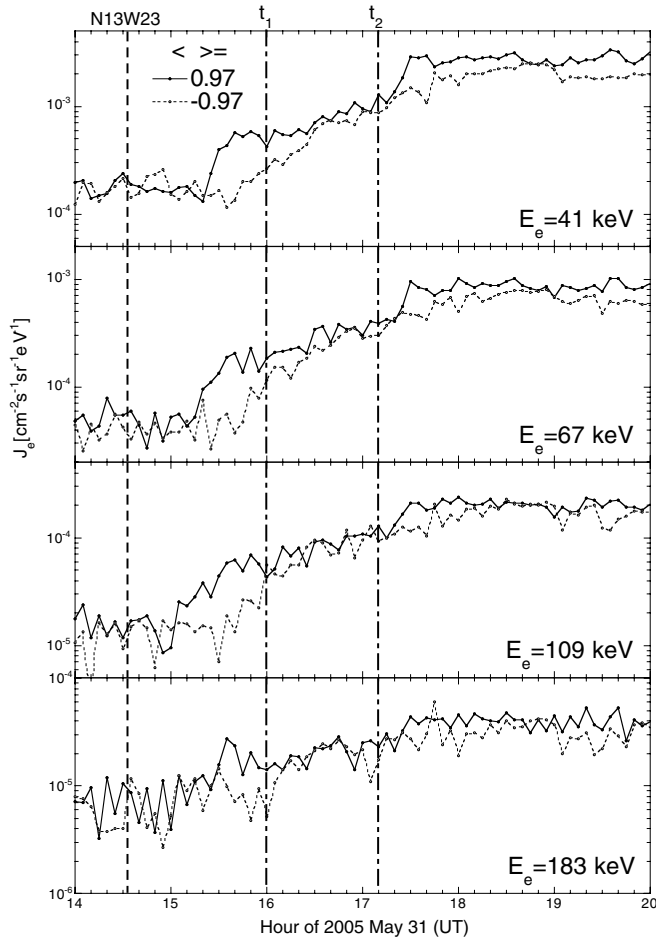


Figure 6. Time profiles of *Wind*/3DP/SST unidirectional electron intensities $J_e(\mu \sim \pm 1)$ data with a time resolution of 5 minutes are shown at selected electron energy (E_e) channels in the 2005 May 31 diffusive electron event, where the vertical dashed line denotes the parent flare. The vertical dot-dashed lines t_1 and t_2 define a more isotropic interval of electrons.

electron energy range, across which the electron transport status changes between scatter free and diffusive, is different from that in the 1999 August 7 impulsive electron event. Assuming that the change occurs between E_1 and E_2 , in the August event we have $E_1 \sim 60$ keV and $E_2 \sim 120$ keV, while in the April event we have $E_1 \sim 250$ keV and $E_2 \sim 500$ keV. The higher E_1 and E_2 values in the April event are consistent with its higher α_p value at very low energies (see Figure 12), indicating a weaker wave scattering environment in the April event. Nevertheless, the ratio of the width of the energy window $\Delta E = E_2 - E_1$ to the mean energy $E_m = (E_2 + E_1)/2$ is still same in the two events: $\Delta E/E_m \sim 2/3$.

2.4.3. Anisotropy in Diffusive Electron Events

For the diffusive electron event it is impractical to examine the electron PAD by using the J_{ep} versus μ plot, because of the difficulty in finding t_p from slowly rising, strongly fluctuating time profiles of J_e . Therefore, in Figure 6 instead of the J_{ep} versus μ plot we show the time profiles of $J_{\mu = 0.97}$ and $J_{\mu = -0.97}$ at selected E_e channels to illustrate the characteristics of diffusive electron event. Here the vertical dot-dashed lines t_1 (16:00 UT) and t_2 (17:10 UT) divide the entire time (t) axis into three segments: (1) at $t < t_1$ electrons presented significant anisotropy that $J_{\mu = 0.97} > J_{\mu = -0.97}$; (2) at $t_1 < t < t_2$ electrons exhibited nearly isotropic distribution that $J_{\mu = 0.97} \sim J_{\mu = -0.97}$; and (3)

at $t > t_2$ as electron intensities increased again their anisotropic distributions that $J_{\mu = 0.97} > J_{\mu = -0.97}$ also restored. We will examine if this change of electron anisotropies is correlated with the variation of IMF PSDs later in this paper.

2.5. Characteristics of PSDs of IMF Fluctuations

2.5.1. Fast-rise–Fast-decay Impulsive Electron Event

We have carried out the PSD analysis by using the *Wind*/MFI magnetic field data with a time resolution of 96 ms. In Figure 7, we show the total PSD spectra during the consecutive time intervals in the 1999 August 7 event. Each panel in the figure includes 32768 (2^{15}) *Wind*/Magnetic Field Investigation (MFI; Lepping et al. 1995) data points covering a time interval of ~ 50 minutes. The total PSD is the summation of three PSD components with the spacecraft spin tone signal removed. For comparison, we also include the *ACE*/Magnetic Field Experiment (MAG; Smith et al. 1998) magnetic field data with the time resolution of 1 s. By using a smooth program given by Stineman (1980), we compute the statistics of the logarithm of the quantity under consideration. According to Bieber et al. (1996), the logarithmic averaging is better than the arithmetic averaging, because it is equivalent to the geometric average, which can avoid the influence of extreme members in the data set. As shown in Figure 7, a fine comparison between the *Wind* and *ACE* observations can be carried out by the examination of smoothed PSD spectra. In fact, during the 1999 August 7 event period both *Wind*/MFI and *ACE*/MAG data were well consistent, in spite of the distance between the two spacecraft was $\sim 140 R_E$. In addition, during the consecutive time intervals shown in Figure 7 the observed spectra of PSDs were nearly unchanged.

The frequency (ν_0) spectrum of total PSDs has a significant steepening at the frequency $\nu_{b0} \sim 0.3$ Hz. In the lower frequency (LF) range ($\nu_0 < \nu_{b0}$) the PSD_l spectrum can be approximated by a power-law function of ν_0 (the thin green line),

$$\log(\text{PSD}_l) = \log(p_l)_0 + b_l \log(\nu_0), \quad (7)$$

where $(p_l)_0$ and b_l are the PSD_l value at $\nu_0 = 1$ Hz (the vertical dashed line in Figure 7) and the LF spectral index of PSD spectrum, respectively. Note that $b_l = -q$ in Equation (1). The PSD data between $\nu_0 = 10^{-2}$ and 10^{-1} Hz (the two vertical green lines) are used in the fitting process of Equation (7).

On the other hand, the *Wind*/MFI flux gate instrument has a flat noise level that is discernable at $\nu_0 > 2$ Hz (A. Szabo 2010, private communication). As a result, in the high-frequency (HF) range the PSD_h spectrum gradually becomes flattened. We hence fit the variation of $\log(\text{PSD}_h)$ versus $\log(\nu_0)$ by a polynomial function of the order of two (the thin purple line):

$$\log(\text{PSD}_h) = \log(p_h)_0 + b_h \log(\nu_0) + c_h \log^2(\nu_0), \quad (8)$$

where c_h is a constant, $(p_h)_0$ and b_h are the PSD_h value and HF spectral index at $\nu_0 = 1$ Hz, respectively. The PSD data between $\nu_0 = 0.5$ –2 Hz (the two vertical purple lines) are used in the fitting process of Equation (8).

We calculate the breaking frequency ν_{b0} by assuming $\text{PSD}_l = \text{PSD}_h$ in Equations (7) and (8). The deduced ν_{b0} value is indicated in Figure 7 by an arrow. It can be seen that during the consecutive time intervals given in Figure 7 $\nu_{b0} \sim 0.3$ Hz with small variations. The $\log(p_h)_0$ value is quite high. Nevertheless, because of a high $\log(p_l/p_h)_0$ value (> 1) the PSD_h value at $\nu_0 > 1$ Hz could quickly approach the noise level. The presence

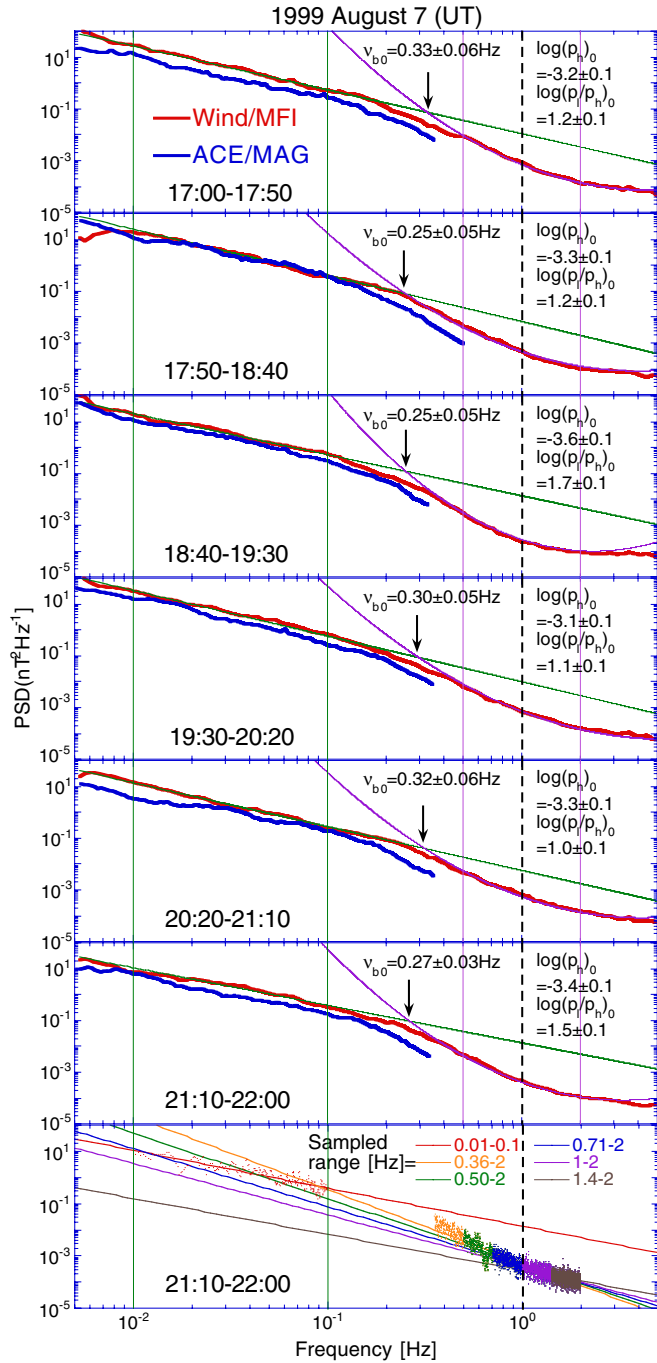


Figure 7. Total PSDs of IMF fluctuations measured by the *Wind*/MFI (red line) and *ACE*/MAG (blue line) are plotted against the wave frequency (ν_0) in the spacecraft frame for the 1999 August 7 event. Each panel corresponds to a ~ 50 minute interval counted from top to bottom along an ascending time order. The green and purple lines exhibit the fitting results of PSD spectra in the lower and higher frequency ranges, which are defined by the vertical green and purple lines, respectively. The arrow indicates the calculated break frequency ν_{b0} of the dissipation range and the vertical dashed line denotes $\nu_0 = 1$ Hz. In addition, on the bottom panel the power-law fits of PSDs in the lower and higher frequency ranges are given, where the thin colored lines denote the power-law fitting results given at different sampled frequency ranges.

of ν_{b0} implicates a strong damping of waves above it. In fact, any strong damping would have led to a much steeper spectrum, if not to a clear cutoff (Stawicki et al. 2001). Thus the spectral steepening could occur at both the proton (ν_p) and electron (ν_e) gyrofrequencies (see Section 3.2). Unfortunately, the noise of

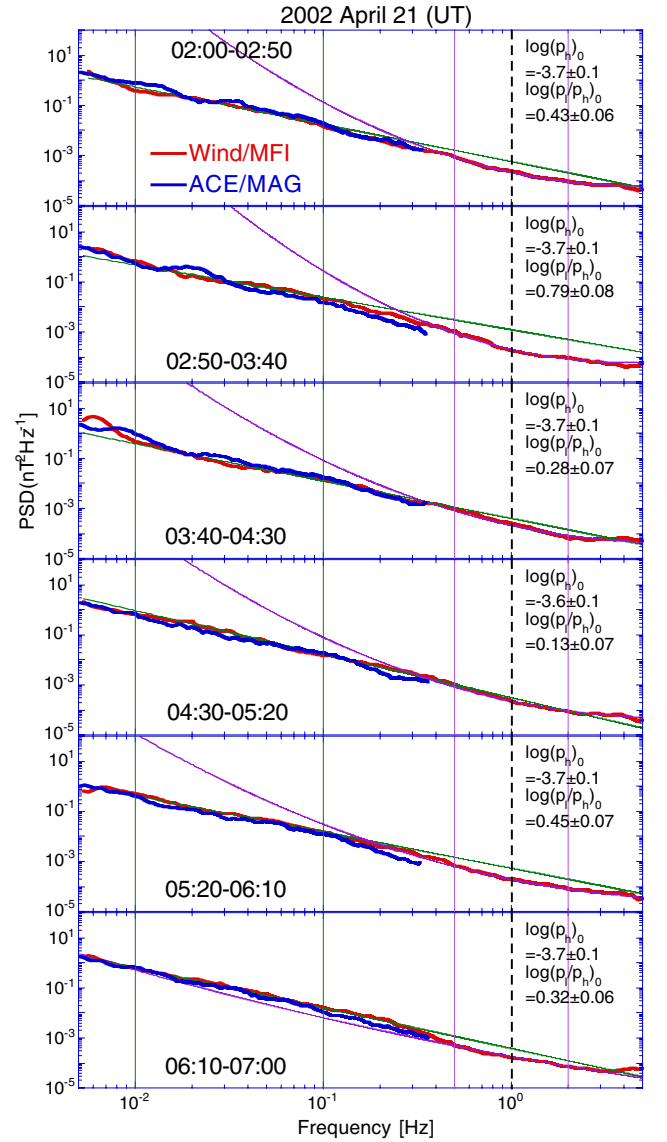


Figure 8. Same as Figure 7, but for the 2002 April 21 event.

the magnetic field instrument usually masks the spectral variation at higher frequencies. Recently, Sahraoui et al. (2009) use both magnetic and electric field data of the *Cluster* spacecraft to examine the spectral steepening at higher frequencies. They observe two distinct breakpoints in the magnetic field PSD spectrum at 0.4 and 35 Hz, which correspond to the Doppler-shifted proton and electron gyroscscales, respectively. In addition, the two breakpoints divide the entire spectrum into three segments, having the slopes -1.62 , -2.3 , and -4.1 from low to high frequencies, respectively. Their deduced two slopes (-1.62 and -2.3) at lower frequencies correspond to our observed $b_l = -1.66$ and $b_h = -2.66$ values in Figure 7, respectively (also see Table 1). In addition, our deduced PSD_h spectrum is flattened at $\nu_0 > 5$ Hz with a magnitude of $\sim 10^4 \text{ nT}^2 \text{ Hz}^{-1}$, which is also similar to their total magnetic spectrum deduced from the flux gate magnetometer (FGM) data on *Cluster* spacecraft (Balogh et al. 2001).

2.5.2. Magnetic Cloud Event

Similarly, we carry out the PSD analysis of the 2002 April 21 MC event. As shown in Figure 8 and Table 1, the main features

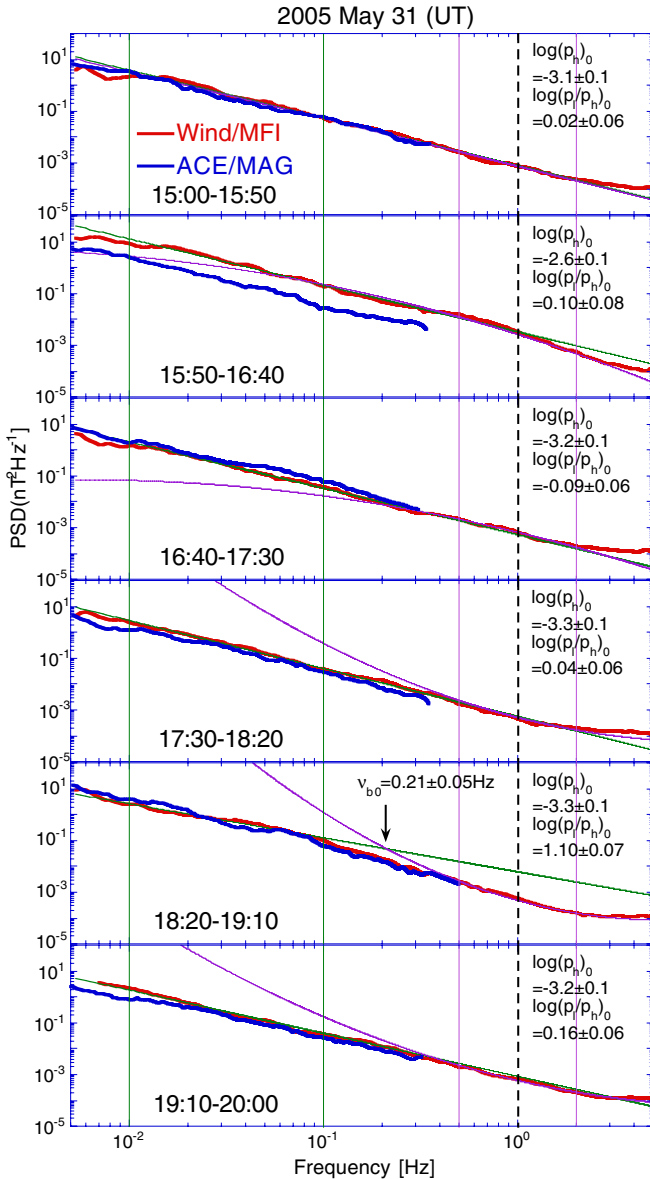


Figure 9. Same as Figure 7, but for the 2005 May 31 event.

of the event are (1) the difference between b_l and b_h or between $(p_l)_0$ and $(p_h)_0$ is small, making it difficult to calculate the ν_{b0} value; (2) although $|b_h|$ is low, yet the PSD_h value at $\nu_0 > 1$ Hz can quickly approach the noise level because of very low value of $(p_h)_0$; and (3) during the consecutive time intervals of the event the spectral shape of PSDs is nearly unchanged.

2.5.3. Diffusive Electron Events

Because of the damping effect of L -mode waves by solar-wind thermal ions, the residual scattering experienced by electrons with a few tens keV energies is mainly due to the R -mode waves in the frequency range between $\nu_0 = 0.1$ and 1 Hz. Therefore, we take $(p_h)_0$ as a proxy of the scattering wave intensity. It can be seen that in the 2005 May 31 event the maximum of $(p_h)_0$ values occurred in the 15:50–16:40 UT interval, with an enhanced factor of ~ 3 compared with the earlier interval. This interval is coincident with the $t_1 < t < t_2$ interval in Figure 6, during which electrons showed a more isotropic distribution. Therefore, as the first time Figures 6 and 9 provide the direct evidence to support that the locally measured IMF fluctuation

spectrum plays a dominant role in affecting the scattering status of non-relativistic solar electrons locally observed (see Section 1.3). In addition, during the examined interval only the PSD level measured by *Wind* increased, while the PSD level measured by *ACE* did not change. In view of the fact that the two spacecraft were close to the L1 point with their separation of $\sim 120 R_E$, the observed difference of PSD values between the two spacecraft indicates that the flux tubes separated by $\sim 120 R_E$ could be very different. In addition, due to the small difference between b_l and b_h and between $(p_l)_0$ and $(p_h)_0$ as in the April event, we could only calculate the ν_{b0} value in the 18:20–19:10 UT interval.

In summary, it is noted that among the three sampled events, the 2005 May 31 event has the highest PSD value at 1 Hz (i.e., $(p_0)_h$), which is consistent with the diffusive transport feature of low-energy (LE) electrons observed in this event.

3. DISCUSSION

For IMF fluctuations at very low frequencies, electromagnetic waves are Alfvén waves propagating away from the Sun with their wave vectors aligned with the mean magnetic field (Jokipii 1966). Since incompressible MHD turbulence cannot exist in one dimension, it is necessary to introduce energetically populated wave vectors that are not aligned with the mean magnetic field (Hamilton et al. 2008). Therefore, the slab component of IMF fluctuations, whose wave vector is aligned with the mean magnetic field, no longer plays an exclusive role in particle scattering (Leamon et al. 1998, 1999). Nevertheless, by reserving the parallel-propagating wave assumption we are able (1) to demonstrate the variation solely caused by changing the wave modes and hence dispersion relations, and (2) to provide an approximate expression applicable to the case of radial magnetic field, where the ion-cyclotron resonance may dominate the wave dissipation (Bieber et al. 1996; Leamon et al. 1999).

3.1. Minimum Energy of Resonant Electrons

Near and above the proton gyrofrequency Ω_p , wave dispersion relations should be changed to be that of both R -mode and L -mode waves (see Figure 1), leading to the change of minimum energy of resonant electrons. In fact, the relativistic Doppler condition for gyroresonance between electrons and electromagnetic waves propagating parallel to the magnetic field (\mathbf{B}) is

$$\omega - kv_{\parallel} = s\Omega_e/\gamma, \quad (9)$$

where $s = 1$ for R -mode and $s = -1$ for L -mode waves, $\gamma = (1 - v^2/c^2)^{-1/2}$ is the relativistic correction factor, and v_{\parallel} is the velocity component of electrons parallel to \mathbf{B} (Summers & Thorne 2003).

From Equation (9) and the dispersion relations of R -mode and L -mode waves in uniform cold plasma (Stix 1992) we can calculate v_{\parallel} of resonant electrons. Following Summers et al. (2007), we first define the dimensionless frequency $x = \omega/|\Omega_e|$ and wave number $y = ck/|\Omega_e|$, Equation (9) is then rewritten as

$$y = (x - s/\gamma)/(\beta\mu), \quad (10)$$

where $\beta = v/c$. Here we only consider the electron–proton (hydrogen) plasma whose dispersion relationship is

$$y^2/x^2 = 1 - b/((x - s)(x + s\varepsilon)), \quad (11)$$

where $\varepsilon = m_e/m_p$ (m_e and m_p are the electron and proton masses, respectively), and $b = (1 + \varepsilon)/\alpha^*$ (see Equation (2)). The velocity

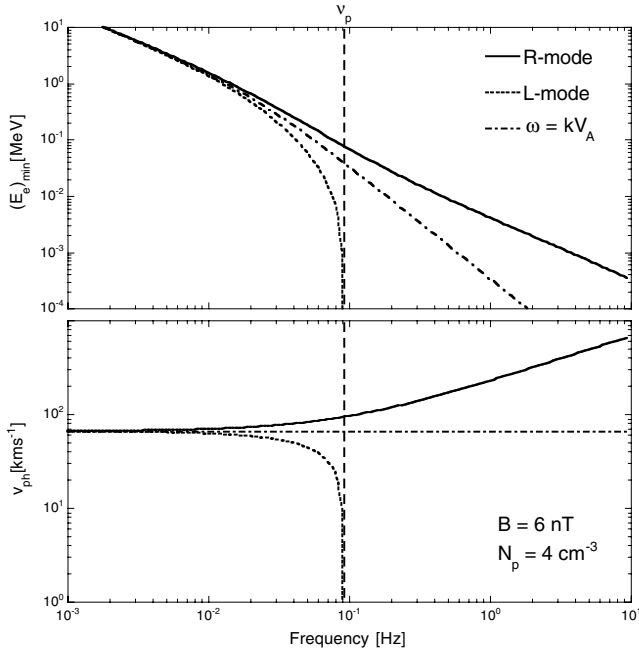


Figure 10. In a typical solar-wind environment observed at 1 AU the wave frequency (ν) plots of the minimum energy ($(E_e)_{\min}$) of resonant electrons (upper panel), and of the phase velocity (V_{ph}) of resonant waves (lower panel) for various electromagnetic wave modes are shown in the plasma frame, where in a uniform cold plasma consisting of protons and electrons the waves are assumed to propagate along the mean magnetic field and ν_p is the proton gyrofrequency.

component parallel to \mathbf{B} , v_{\parallel} , of resonant electrons is

$$v_{\parallel}/c = (xy - s(1 + y^2 - x^2)^{1/2})/(1 + y^2). \quad (12)$$

Addition of He ions into the solar-wind composition would increase an absorption band at lower frequencies (Summers & Thorne 2003), causing an increase of the electron threshold energy, above which the Alfvén wave approximation is available and electrons experience normal scattering.

In the presence of a velocity component perpendicular to \mathbf{B} (i.e., $\mu < 1$) v_{\parallel} corresponds to the minimum energy of resonant electrons:

$$(E_e)_{\min} = (m_e c^2)((1 - v_{\parallel}^2/c^2)^{-1/2} - 1). \quad (13)$$

When $\mu = 1$, $(E_e)_{\min} = E_e$. For the typical electron scatter-free transport events observed at 1 AU (i.e., $B = 6$ nT and $N_p = 4$ cm $^{-3}$, see Table 1) the deduced $(E_e)_{\min}$ is plotted against ν for the R -mode, L -mode, and Alfvén waves in the upper panel of Figure 10. It appears that at $(E_e)_{\min} > 500$ keV electrons indeed experience normal scattering by Alfvén waves, which explains the common absence of scatter-free transport events of relativistic electrons.

In the lower panel of Figure 10 the phase velocity V_{ph} of these waves is shown. Note that when $\nu = \omega/2\pi$ approaches $\nu_p = \Omega_p/2\pi$ from the lower frequency end, the V_{ph} value of L -mode waves quickly approaches zero, indicating the disappearance of L -mode waves. The wave disappearance opens the possibility of scatter-free propagation of LE electrons. On the other hand, the wave disappearance causes the observable spectral steepening of IMF fluctuations in the dissipation range.

It should be mentioned that in the slab turbulence model the propagation direction and polarization of transverse electromagnetic circularly polarized plane waves are important parameters

to distinguish between different wave modes. While their detailed description is beyond the scope of this paper, their effect on the scattering status of non-relativistic solar electrons cannot be ignored. Here we use + and - to denote the wave propagation directions away from and toward the Sun along the IMF, respectively. Also, we use R and L to denote the right-hand and left-hand polarization wave modes, respectively. Thus wave modes with different propagation directions and polarizations should reside in different quadrants in the k - ω plane, while in Figure 1 they are simply put on the same quadrant.

Based on their gyrating direction, protons streaming outward (+) can only be resonant with $R+$ and $L-$ waves (Ng & Reames 1995). In fact, outward traveling protons amplify the outward $R+$ mode waves and damp the inward $L-$ mode waves. In contrast, electrons streaming outward (+) can only be resonant with $L+$ and $R-$ waves. Outward traveling electrons amplify the outward $L+$ mode (EMIC) waves and damp the inward $R-$ mode (whistler) waves. However, since at frequencies above ν_p the $L+$ waves are heavily damped by solar-wind thermal ions (i.e., these waves are essentially non-existent; see the next section), there should be a lack of scattering of LE electrons by the $L+$ waves. On the other hand, LE electrons can also be resonant with $R-$ mode (whistler) waves. The $R-$ waves will most likely be damped by the outward streaming electrons themselves if the waves were large; if they were small, damping would not matter as far as electron transport is concerned. Thus the above description explains why electrons of sufficiently LEs run out of resonant waves and may experience the scatter-free transport in the interplanetary space.

3.2. Beginning Frequency of Dissipation Range

We consider the damping effect of $L+$ mode waves by solar-wind thermal ions. Being different from solar energetic ions that are streaming outward from the Sun, solar-wind thermal ions have an isotropic distribution in the solar-wind frame. Because of the frozen-in assumption (Leamon et al. 1998), the solar-wind frame is the plasma frame. As a result, inward streaming solar-wind thermal protons amplify the inward $R-$ mode waves and damp the outward $L+$ mode waves, causing the steepening of frequency spectra of PSDs in the dissipation range.

Here we make a re-estimation of the breaking frequency ω_b of the dissipation range still based on the slab model, because in the previous estimation (e.g., Leamon et al. 1998) we had noted that some factors, which may affect the result of the estimation, could be questionable. For example, previously the breaking frequency was determined by fitting the lower frequency and higher frequency parts of the PSD spectrum with the power-law function separately. While the *Wind*/MFI magnetometer data indicate the instrumental noise that is nominally discernable at > 2 Hz (A. Szabo 2010, private communication), the estimated power-law function of the higher frequency part under the assumed upper frequency limit of 2 Hz is found to be dependent upon the lower frequency limit (see the bottom panel of Figure 7), leading to the uncertainty of the deduced breaking frequency that also depends on the lower frequency limit in the estimation of the higher frequency power-law function. In addition, previously in the calculation of breaking frequency, the dispersion relation of Alfvén waves was used as an approximation. Because of the rapid change of the wave phase velocity near the proton gyrofrequency, the dispersion relation of the EMIC waves should be used instead. A question has hence arisen whether or not the slab model can make a reasonable estimation of the breaking frequency after having corrected

these factors. For inward traveling thermal protons with outward propagating $L+$ mode waves, the resonance condition that

$$\omega_b + kv_p = \Omega_p \quad (14)$$

gives the minimum resonant wave number, where v_p is the proton velocity (Leamon et al. 1998). In order to deduce ω_b , hereafter we assume $v_p = v_{th}$, the average thermal velocity of solar-wind ions derived from the solar-wind temperature (T).

In addition, note that in Equation (2) of Leamon et al. (1998) the dispersion relation of Alfvén waves (i.e., $\omega = kV_A$) is used, leading to that

$$\omega_b = \Omega_p / (1 + v_{th}/V_A). \quad (15)$$

However, since ω_b is close to Ω_p , the dispersion relation of L -mode waves must be taken into account. Correspondingly, instead of Equation (15) we should have

$$\omega_b = \Omega_p / (1 + v_{th}/V_{ph}(\omega_b)), \quad (16)$$

where the phase speed of waves $V_{ph} = c\gamma/\omega$ can be estimated from Equation (11). Thus, an iteration procedure is designed to calculate ω_b . Finally, in view of the Doppler shift, the beginning frequency $\nu_{b0} = \omega_{b0}/2\pi$ of the dissipation range predicted in the spacecraft frame is

$$\nu_{b0, \text{pred}} = \nu_p (1 + (V_{sw}/V_{ph}(\omega_b)) \cos \theta_{Bsw}) / (1 + v_{th}/V_{ph}(\omega_b)), \quad (17)$$

where θ_{Bsw} is the angle between the wave number vector that is assumed aligned with \mathbf{B} and the solar-wind velocity vector.

From Table 1 it can be seen that the breaking frequency predicted by the improved slab model calculation could be consistent with observations. In addition, we have analyzed the solar-wind data during the 2006 March 19 20:30–23:20 UT interval as examined by Sahraoui et al. (2009). By substituting the observed solar-wind parameters $B = 5.8 \pm 0.9$ nT, $N_p = 3.2 \pm 0.6$ cm⁻³, $v_{th} = 63 \pm 17$ km s⁻¹, $V_{sw} = 660 \pm 20$ km s⁻¹, and $\cos \theta_{Bsw} = 0.73 \pm 0.24$ into Equation (17), we obtain $\nu_{b0, \text{pre}} = 0.42 \pm 0.15$ Hz, which is also consistent with $\nu_{b0, \text{obs}} \sim 0.4$ Hz found by Sahraoui et al. (2009). Thus an improved slab model calculation could provide an approximate estimation of the breaking frequency, implying that this simplistic model may contain a rational kernel in the real theory.

3.3. Implication of Electron Scattering Status Change

Here we explain the implication of the observed change of electron scattering status occurring in an energy window ΔE , where $\Delta E \sim 2E_m/3$ and E_m is the mean energy at which the electron scattering status changes (see Section 3.1). Because of the r -dependence of B we ought to expect $\nu_p \propto B \propto r^{-2}$. Thus at small r values the ν_p value and its corresponding $(E_{eb})_{\min}$ value should be significantly different from that observed at 1 AU. Therefore, if the change of electron scattering status occurred in a large r range, the integrated effect of different $(E_{eb})_{\min}$ values along r would blur the E_e variation of electron scattering status, making it impossible to observe any drastic change of the status. The observed fact that a drastic change of electron scattering status occurring at ΔE indicates that only in a limited Δr range electron scattering could affect the observation at 1 AU.

We estimate Δr for non-relativistic electrons. With $\omega \ll kv_{\parallel}$ from Equation (9) we have

$$v_{\parallel} \approx \Omega_e / (\gamma k). \quad (18)$$

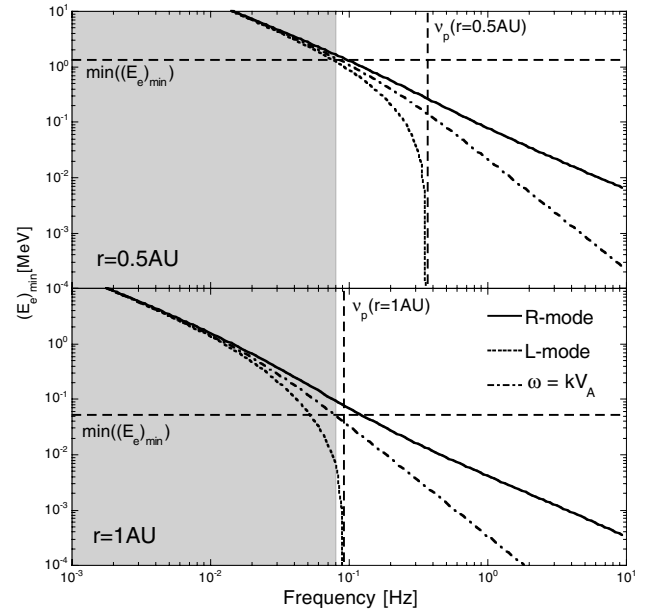


Figure 11. Minimum energy $((E_e)_{\min})$ of resonant electrons is plotted against the wave frequency (ν) in the plasma frame, where the lower panel is reproduced from the upper panel of Figure 10, while the upper panel is calculated by taking into account of the radial variation of B and N_p . The shaded gray region denotes the equivalent PSD range and $\min((E_e)_{\min})$ is the minimum of $((E_e)_{\min})$, above which electrons may experience normal scattering by Alfvén waves (see the text).

Under the Alfvén wave approximation (Equation (3)) and $\gamma \sim 1$ we have

$$\beta \approx (\Omega_e/\omega)(V_A/c). \quad (19)$$

At $\omega \approx \Omega_p$, we have $\beta \propto V_A \propto B/N_p^{1/2}$, where N_p is the number density of solar-wind protons. Since the heliospheric density model predicts $N_p \propto r^{-2.1}$ (Mann et al. 1999), we have $V_A \propto r^{-1}$ and $(E_{eb})_{\min} \propto \beta^2 \propto r^{-2}$. Therefore, $\Delta r/r \approx (\Delta(E_{eb})_{\min}/(E_{eb})_{\min})/2$. Assuming that $\Delta(E_{eb})_{\min}/(E_{eb})_{\min} \sim \Delta E/E_m$, we obtain $\Delta r/r \sim 1/3$ or $\Delta r \sim 0.3$ AU at $r \sim 1$ AU. Actually, in view of the roughness of the Δr deduction process, the above estimation implies that only IMF fluctuations at $r \geq 0.5$ AU could affect the electron PAD observed at 1 AU. As explained in Section 1.2, the physical reason causing such a limitation is due to the coexistence of the particle adiabatic focusing effect, which may always dominate over scattering at smaller r -value to give a beam-like particle angular distribution implying a nearly scatter-free propagation (Lin 1985).

In order to explore the difference of electron scattering status between $r = 0.5$ AU and 1 AU, the wave frequency dependence of the minimum energy of resonant electrons $((E_e)_{\min})$ as calculated at $r = 1$ AU is compared with that at $r = 0.5$ AU in Figure 11, where the lower panel is reproduced from the upper panel in Figure 10, while the upper panel is the calculation result taking into account of the radial dependence that $B \propto r^{-2}$ and $N_p \propto r^{-2}$. Because of $\nu_p \propto B$, ν_p at $r = 0.5$ AU is four times the value of ν_p at $r = 1$ AU, leading to a significant difference of the wave frequency dependence of $(E_e)_{\min}$ between the two radial locations in the plasma frame.

On the other hand, the magnetic field PSD spectrum does not exhibit any significant difference between the two radial locations. By using the *Helios* magnetic field data, Wanner (1993) made a detailed examination of the radial variation of magnetic field PSDs between $r = 0.3$ and 1 AU. His main findings include (1) the spectral slope q in the inertial range is

nearly unchanged (see his Figure 4.24); (2) while the magnetic field power integrated over a frequency range decreases with the increase of r , the ratio of the power (p_r) to B^2 is nearly unchanged (see his Figure 4.22). Note that in Equation (1) the strength of particle scattering A is mainly dependent upon the ratio p_r/B^2 .

Therefore, from Wanner (1993) it can be seen that the magnetic field PSDs with the same strength of particle scattering (the “equivalent” PSDs) appear in the same frequency range between $r = 0.5$ and 1 AU. From Figure 7 the upper boundary of this equivalent PSD region can be set at $\nu_{b0} \sim 0.3$ Hz in the spacecraft frame. Under the average solar-wind condition ($V_{sw} = 400 \text{ km s}^{-1}$ and $\theta_{Bsw} = 45^\circ$) we can reduce this upper boundary to be 0.08 Hz in the solar-wind frame. Thus, in Figure 11 we use the shaded gray region to denote the frequency range in which solar electrons would experience normal scattering by Alfvén waves. The upper frequency limit of the region determines the minimum of the minimum energy of resonant electrons ($\min((E_e)_{\min})$), above which electrons could experience normal scattering. Thus, from Figure 11 it can be seen that from $r = 0.5$ AU to 1 AU the $\min((E_e)_{\min})$ value decreases from 1.3 MeV to 50 keV. Consequently, electrons with energies of 0.05–1.3 MeV should change their scattering status between $r = 0.5$ and 1 AU.

In addition, it is interesting to examine the radial variation of SEP intensities observed on the *Helios* spacecraft. The lowest energy channel (E03) of electrons as detected by *Helios* is 0.3–0.8 MeV (Wibberenz et al. 1989). However, an accurate Monte Carlo calculation, in which large-angle scattering of the electrons is taken into account, leads to a characteristic mean energy of this channel being 0.95 MeV (Wibberenz & Cane 2006), which is close to the $\min((E_e)_{\min})$ value at $r = 0.5$ AU. Therefore, it is not surprising that one may observe the diffusive transport event of ~ 1 MeV electrons at $r \sim 0.5$ AU. Our concern, however, is the “fate” of those scatter-free electron transport events observed at ~ 0.5 AU. We argue that at lower energies (~ 0.1 MeV) these events would keep their scatter-free transport feature at 1 AU, while at higher energies (~ 1 MeV) they should change to diffusive transport at 1 AU. Our argument is consistent with the observed absence of scatter-free transport event of relativistic electrons at 1 AU (Lin 1974), where only scatter-free transport events of ions are found (Mason et al. 1989; Tan & Mason 1993).

3.4. Broken Power-law Spectra of Solar Electrons

In Section 2.4.1, we have observed that in the 1999 August 7 and 2002 April 21 events the transition of electron scattering status from scatter free to diffusive occurs within the *Wind*/3DP/SST measured energy range (25–500 keV) with $\Delta E/E_m \sim 2/3$ and E_m is event dependent. While the events are observed in their entirety, it is more interesting to examine the characteristics of the peak electron intensity J_{ep0} (see Equation (4)) in each event, because the impulsive diffusion model (Parker 1963) may be used to give some hints of the implication of J_{ep0} observations. Therefore, in the upper panel of Figure 12 we summarize the observed results of $\alpha_p = d\ln(J_{ep})/d\mu$, whose increases indicate the shrinking of electron PADs toward $\mu = 1$, for the two events shown in Figures 3 and 4. Here the solid dot and open circle express the 1999 August 7 impulsive and 2002 April 21 MC events, respectively. Also, the horizontal solid and dashed lines denote $\alpha_p = 3.0$ and 1.5, respectively. It can be seen that the transition region $\Delta E = E_2 - E_1$ of electron scattering status occurred at $E_1 = 60$ and $E_2 = 120$ keV for the

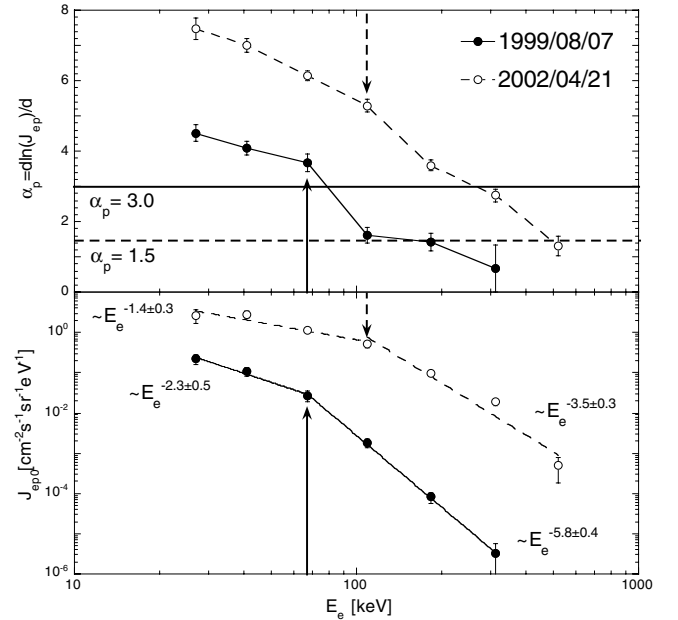


Figure 12. Electron energy (E_e) dependence of $\alpha_p = d\ln(J_{ep})/d\mu$ (upper panel), whose increase indicates the shrink of peak electron PADs toward $\mu = 1$, and J_{ep0} , the maximum peak electron intensity given at $\mu = 1$ (lower panel) in the 1999 August 7 and 2002 April 21 events. The solid and dashed arrows indicate the energies at which the electron energy spectrum is broken into two power-law segments in the August and April events, respectively.

August event, and $E_1 = 250$ and $E_2 = 500$ keV for the April events.

What is the effect of the change of electron scattering status on the shape of electron energy spectra? It is well known that the electron peak intensity spectrum generally shows a broken power-law dependence with the spectral steepening occurring at $E_e \approx 60$ keV. However, it is unclear if the steepening is caused by electron acceleration processes or due to transport effects (Krucker et al. 2009). We hence plot the maximum magnitude (J_{ep0}) spectrum of peak electron intensities for the two events in the lower panel of Figure 12, where the two spectra are clearly broken at $E_{eb} \sim 65$ keV and 110 keV, as indicated by the solid and dashed arrows for the August and April events, respectively. In the August event, the spectral indices deduced by us are consistent with those by Wang et al. (2006), who found that the LE and high-energy (HE) spectral indices are respectively -2.94 and -4.55 , in comparison with -2.3 and -5.8 shown in Figure 11, respectively. For the April event the LE and HE spectral indices are -1.4 ± 0.3 and -3.5 ± 0.3 , respectively. While the difference between LE and HE spectral indices is less than that in the August event, the spectral breaking is statistically significant. Therefore, the spectral steepening is not unique for impulsive electron events. As described in Section 2.4.2, assuming the change of scattering status occurring between E_1 and E_2 , we have $E_1 \sim 60$ keV and $E_2 \sim 120$ keV in the August event, and $E_1 \sim 250$ keV and $E_2 \sim 500$ keV in the April event. Comparing with the LE spectrum below E_{eb} , we have noted that in the two events J_{ep0} at E_2 experiences an additional decrease of ~ 1 order of magnitude due to the spectral steepening.

Furthermore, from the upper panel of Figure 12 it can be seen that the departure from the LE slow variation trend of α_p occurs above E_{eb} , where α_p is rapidly decreased with increasing E_e . Therefore, the transition of electron scattering status is correlated with the breaking of electron power-law energy spectra. It is understandable if one considers that in the

two events a beam-like particle angular distribution implying a scatter-free propagation ($\lambda > 1$ AU) always exists at $r < 0.5$ AU (see Section 3.3), while in the local environment we observe the scatter-free transport ($\lambda > 1$ AU) at lower energies and diffusive transport ($\lambda < 0.5$ AU) at higher energies. Consequently, above E_{eb} the β factor in Equation (5) plays an important role in affecting the spectral shape. In fact, at lower energies $\beta \sim 0$ because electrons keep scatter-free transport status, while at higher energies $\beta \sim 2$, as seen from MeV proton simulations (see Figure 2 of Ng et al. 2003). Since at higher energies electrons would experience normal scattering by Alfvén waves like MeV protons, the radial variation trend of λ for the electrons should be similar to that for MeV protons. In the spherically symmetric radial diffusion model with an impulsive electron injection (Parker 1963) for a given E_e channel the peak electron intensity of J_{ep0} is

$$J_{ep0}(r) \sim \frac{N}{4\pi r^3} \left[\frac{3(2-\beta)}{2\pi} \right]^{1/2}, \quad (20)$$

where N is a constant related to the source strength (also see Ng & Reames 1994). From Equation (20) the $4\pi r^3 J_{ep0}(r)/N$ value is equal to 0.93 for $\beta = 0$, 0.22 for $\beta = 1.9$, and vanishes at $\beta \rightarrow 2$. Therefore, at E_2 the β factor should be sufficient to generate an additionally decrease of J_{epm} by ~ 1 order of magnitude. Thus the J_{epm} spectral steepening above E_{eb} may be correlated with the change of electron scattering status.

3.5. Comparison of Electron Transport Effect Caused by Electrostatic Electron Plasma Waves with that Caused by Electromagnetic Waves

Recently, Kontar & Reid (2009) simulated the transport of solar energetic electrons in the heliospheric plasma by taking into account of the beam-driven electrostatic electron plasma (Langmuir) wave and solar-wind density inhomogeneity. Their simulation shows a break of peak electron intensity spectra in the case that the injected electron spectrum is a single power law in shape. Also, below the spectral breaking energy there should be an apparently early onset of electron injection, which may originate from the wave-particle interaction that causes in-flight deceleration of electrons. In contrast, since higher energy electrons cannot excite turbulences because of their low intensity, they should experience scatter-free transport.

In the simulation of Kontar & Reid (2009) the effect of electromagnetic waves has been ignored. On the other hand, we have not taken into account the effect of the electrostatic electron plasma (Langmuir) waves. Therefore, the two works, which consider the effects of different wave modes, may be complementary to each other and effective in different electron energy ranges.

Let us explain this complementarity by taking the 1999 August 7 event as an example. It can be seen from Figure 4 in Wang et al. (2006) and Figure 12 in this work that the breaking of peak electron intensity spectra occurs at $E_{eb} \sim 65$ keV, above which electrons gradually change to the diffusive transport because of wave scattering (see Figure 3). Therefore, the conclusion made by Kontar & Reid (2009) that above E_{eb} electrons would experience scatter-free transport is inconsistent with observations. However, it is possible that the breaking energy predicted by Kontar & Reid (2009) should occur at E_e much lower than 65 keV. In fact, Figure 4 in Kontar & Reid (2009) indicates that below the breaking energy electrons should exhibit apparently early onset of injection. Since only below

~ 25 keV electrons exhibit early onset of injection according to Wang et al. (2006), the breaking energy predicted by Kontar & Reid (2009) should be below ~ 25 keV. Therefore, electrons at $E_e = 25$ –65 keV belong to the “high-energy” range in the simulation of Kontar & Reid (2009). From Figures 3 and 12 in this paper it can be seen that electrons at $E_e = 25$ –65 keV indeed experience scatter-free transport as expected for HE electrons in the simulation of Kontar & Reid (2009).

Therefore, in view of the observational fact that electrons above ~ 25 keV show a simultaneous solar injection, further change of peak intensity spectra of solar electrons as suggested by Kontar & Reid (2009) could occur below ~ 25 keV. We expect to examine the change in the future by using the electron electrostatic analyzer (EESA-H) data obtained from the *Wind*/3DP instrument.

4. SUMMARY

We have analyzed the reasons causing the scatter-free transport of non-relativistic solar electrons. Our main findings are as follows.

1. For our representative fast-rise-fast-decay impulsive electron event and magnetic cloud event we have observed that the PAD of electrons is electron energy (E_e) dependent. The transition of electron scattering status from scatter free to diffusive occurs within the *Wind*/3DP/SST measured range (25–500 keV) with $\Delta E/E_m \sim 2/3$ and E_m is event dependent.
2. The electron breaking energy, at which the observed electron energy spectrum is broken into two power-law segments, corresponds to the electron energy, above which the electron PAD changes abruptly. Therefore, the breaking of electron energy spectra could be correlated with the change of electron scattering status.
3. Since near and above the proton gyrofrequency the electromagnetic waves propagating along the magnetic field consist of both R -mode (whistler) and L -mode (EMIC) waves, the spectral steepening of IMF PSDs due to the EMIC wave damping by solar-wind thermal ions becomes essential. In a typical fast-rising-fast-falling impulsive electron event we have observed such steepening, which signifies the occurrence of scatter-free transport of LE electrons.
4. By analyzing IMF fluctuations in consecutive time intervals during the scatter-free transport period of solar electrons, we have noted that the magnitude of PSD spectra is nearly time independent since the event onset. In contrast, in the diffusive transport event the enhancement of IMF PSDs is correlated with the appearance of more isotropic electron angular distributions, indicating that locally measured IMF fluctuation spectrum plays a dominant role in affecting the observed scattering status of non-relativistic solar electrons.
5. It appears that the scatter-free propagation of non-relativistic electrons is due to a negligible magnetic fluctuation level in the spacecraft frequency range of $\nu_0 = 0.1$ –1 Hz. Therefore, based on our analysis we conclude that in the 2002 April 21 MC event, non-relativistic electrons should experience scatter-free transport. The observed anisotropic distribution of solar electrons in the event is in support of our conclusion.
6. In summary, there exists a connection between the transition from diffusive to scatter-free electron transport and the concurrent transition from high to low IMF PSD levels

with corresponding breaks in the electron power-law energy spectrum and PSD spectrum.

We gratefully acknowledge data provided by the NASA/Space Physics Data Facility (SPDF) CDAWeb, *ACE* Science Center, and *Wind*/3DP Data Center. We thank A. Szabo for making the *Wind*/MFI high-resolution data available to this work. Also, we thank K. Ogilvie, R. Lin, and A. Szabo for their support of this work, and the anonymous reviewer for his/her valuable comments. L.C.T. is supported in part by NASA grant NNX10AE90G. D.V.R. is supported in part by NASA grant NNX08AQ02G. C.K.N. is supported in part by NASA grant NNX09AU98G. X.S. is supported in part by NASA grant NNX07AF42G. L.W. is supported in part by NASA grant NNX08AE34G.

REFERENCES

- Achatz, U., Dröge, W., Schlickeiser, R., & Wibberenz, G. 1993, *J. Geophys. Res.*, **98**, 13261
- Balogh, A., et al. 2001, *Ann. Geophys.*, **19**, 1207
- Bieber, J. W., Matthaeus, W. H., Smith, C. W., Wanner, W., Kallenrode, M. B., & Wibberenz, G. 1994, *ApJ*, **420**, 294
- Bieber, J. W., Wanner, W., & Matthaeus, W. H. 1996, *J. Geophys. Res.*, **101**, 2511
- Buttighoffer, A., Thomson, D. J., MacLennan, C. G., & Forsyth, R. J. 1999, *A&A*, **351**, 385
- Coleman, P. J., Jr. 1966, *Phys. Rev. Lett.*, **17**, 207
- Coleman, P. J., Jr. 1968, *ApJ*, **153**, 371
- Dröge, W. 2003, *ApJ*, **589**, 1027
- Dröge, W., & Kartavykh, Y. Y. 2009, *ApJ*, **693**, 69
- Goldreich, P., & Sridhar, S. 1995, *ApJ*, **438**, 763
- Hamilton, K., Smith, C. W., Vasquez, B. J., & Leamon, R. J. 2008, *J. Geophys. Res.*, **113**, A01106
- Hasselmann, K., & Wibberenz, G. 1968, *Z. Geophys.*, **34**, 353
- Horbury, T. S., Forman, M., & Oughton, S. 2008, *Phys. Rev. Lett.*, **101**, 175005
- Jokipii, J. R. 1966, *ApJ*, **146**, 480
- Jokipii, J. R. 1971, *Rev. Geophys.*, **9**, 27
- Kontar, E. P., & Reid, H. A. 2009, *ApJ*, **695**, L140
- Krucker, S., Oakley, P. H., & Lin, R. P. 2009, *ApJ*, **691**, 806
- Larson, D. E., et al. 1997, *Geophys. Res. Lett.*, **24**, 1911
- Leamon, R. J., Smith, C. W., Ness, N. F., Matthaeus, W. H., & Wong, H. K. 1998, *J. Geophys. Res.*, **103**, 4775
- Leamon, R. J., Smith, C. W., Ness, N. F., & Wong, H. K. 1999, *J. Geophys. Res.*, **104**, 22331
- Lepping, R. P., et al. 1995, *Space Sci. Rev.*, **71**, 207
- Lin, R. P. 1974, *Space Sci. Rev.*, **16**, 189
- Lin, R. P. 1985, *Sol. Phys.*, **100**, 537
- Lin, R. P., et al. 1995, *Space Sci. Rev.*, **71**, 125
- Mann, G., Jansen, F., MacDowall, R. J., Kaiser, M. L., & Stone, R. G. 1999, *A&A*, **348**, 614
- Mason, G. M., Ng, C. K., Klecker, B., & Green, G. 1989, *ApJ*, **339**, 529
- Matthaeus, W. H., & Goldstein, M. L. 1982, *J. Geophys. Res.*, **87**, 6011
- Matthaeus, W. H., Goldstein, M. L., & Reberts, D. A. 1990, *J. Geophys. Res.*, **95**, 20673
- Ng, C. K., & Reames, D. V. 1994, *ApJ*, **424**, 1032
- Ng, C. K., & Reames, D. V. 1995, *ApJ*, **453**, 890
- Ng, C. K., Reames, D. V., & Tylka, A. J. 2003, *ApJ*, **591**, 461
- Parker, E. N. 1963, *Interplanetary Dynamical Process* (New York: Interscience)
- Qin, G., Zhang, M., Dwyer, J. R., & Rassoul, H. K. 2004, *ApJ*, **609**, 1076
- Reames, D. V. 2009, *ApJ*, **693**, 812
- Reames, D. V., Kahler, S. W., & Tylka, A. J. 2009, *ApJ*, **700**, L196
- Richardson, I., & Cane, H. 2010, *Sol. Phys.*, **264**, 189
- Roelof, E. C. 1969, in *Lectures in High Energy Astrophysics*, ed. H. Ogelmann & J. R. Wayland (NASA SP-109; Washington, DC: NASA), 111
- Sahraoui, F., Goldstein, M. L., Robert, P., & Khotyaintsev, Yu. V. 2009, *Phys. Rev. Lett.*, **102**, 231102
- Schlickeiser, R. 1988, *J. Geophys. Res.*, **93**, 2725
- Schlickeiser, R. 1989, *ApJ*, **336**, 243
- Smith, C. W., Acuña, M. H., Burlaga, L. F., L'Heureux, J., Ness, N. F., & Scheifele, J. 1998, *Space Sci. Rev.*, **86**, 613
- Smith, C. W., Hamilton, K., Vasquez, B. J., & Leamon, R. J. 2006, *ApJ*, **645**, L85
- Stawicki, O., Gary, S. P., & Li, H. 2001, *J. Geophys. Res.*, **106**, 8273
- Stineman, R. W. 1980, *Creat. Comput.*, **6**, 54
- Stix, T. H. 1992, *Waves in Plasmas* (College Park, MD: AIP)
- Summers, D., Ni, B., & Meredith, N. P. 2007, *J. Geophys. Res.*, **112**, A04206
- Summers, D., & Thorne, R. M. 2003, *J. Geophys. Res.*, **108**, 1143
- Tan, L. C., & Mason, G. M. 1993, *ApJ*, **409**, L29
- Tan, L. C., Reames, D. V., & Ng, C. K. 2008, *ApJ*, **678**, 1471
- Tan, L. C., Reames, D. V., Ng, C. K., Saloniemi, O., & Wang, L. 2009, *ApJ*, **701**, 1753
- Torsti, J., Riihonen, E., & Kocharov, L. 2004, *ApJ*, **600**, L83
- Tylka, A. J., Cohen, C. M. S., Dietrich, W. F., Lee, M. A., MacLennan, C. G., Mewaldt, R. A., Ng, C. K., & Reames, D. V. 2005, *ApJ*, **625**, 474
- Tylka, A. J., Cohen, C. M. S., Dietrich, W. F., Lee, M. A., MacLennan, C. G., Mewaldt, R. A., Ng, C. K., & Reames, D. V. 2006, *ApJS*, **164**, 536
- von Rosenvinge, T. T., et al. 1995, *Space Sci. Rev.*, **71**, 155
- Wang, L., Lin, R. P., Krucker, S., & Gosling, J. T. 2006, *Geophys. Res. Lett.*, **33**, L03106
- Wanner, W. 1993, *Doctoral thesis*, Christian-Albrechts Univ., Kiel
- Wibberenz, G., & Cane, H. V. 2006, *ApJ*, **650**, 1199
- Wibberenz, G., Kecskeméty, K., Kunow, H., Somogyi, A., Iwers, B., Logachev, Yu. I., & Stolpovskii, V. G. 1989, *Sol. Phys.*, **124**, 353